Interlayer single-atomic Fe−N₄ sites on carbon-rich graphitic carbon nitride for notably enhanced photo-Fenton-like catalytic oxidation processes towards recalcitrant organic micropollutants

Lang Qin, Jiaqi Meng, Guang Yang, Yue Pan, Xinchun Gao, Yuxin Yang [*], Yihang Guo [*]

School of Environment, Northeast Normal University, Changchun 130117, PR China

ABSTRACT

Glucose-assisted supramolecule self-assembly of melamine and cyanuric acid in the presence of $Fe(NO_3)_3$ combined with thermal polymerization is designed to fabricate C-rich g-C_3N_4-embedded interlayer single-atomic Fe−N₄ sites catalyst (Fe_1/C-CN). Fe_1/C-CN exhibits outstanding photo-Fenton-like catalytic oxidation activity towards typical recalcitrant organic micropollutants. For example, the pseudo-first-order kinetic constant of Fe_1/C-CN photo-Fenton-like system is 7.5 and 21.1 times higher than Fe_1/C-CN photocatalysis and Fenton-like systems in degradation of *p*-nitrophenol, and TOC removal efficiency reaches up to 100% after reaction proceeds for 4 h. Mechanism studies reveal that synergy of maximum Fe atom utilization efficiency and boosted photoexcited charge separation dynamics accelerates regeneration of ≡Fe(II) and efficient H_2O_2 activation of Fe_1/C-CN, leading to plentiful active oxygen species for deep oxidation of organic micropollutants. Fe_1/C-CN also shows a robust reusability in long-term remediation of organic micropollutants, attributing to interlayer Fe−N coordination interactions for preventing single Fe atoms from agglomeration and leaching to reaction media.

1. Introduction

Advanced oxidation processes show particular research interests and great application potentials for the remediation of recalcitrant and toxic organic pollutants in wastewater depending on the generated highly reactive oxygen species (ROSs), in which sustainable photocatalysis and heterogeneous Fenton-like processes are the most promising technologies [1]. Nevertheless, both technologies generally suffer from fatal drawback of poor deep oxidation to organic micropollutants due to the sluggish photogenerated charge separation and transfer dynamics for photocatalysis and low activation efficiency of H_2O_2 because of slow surface reduction reaction rate of Fe^{3+} to Fe^{2+} for H_2O_2-based Fenton process [2,3]. Accordingly, the number of the generated hydroxyl radicals (•OH) is limited. The lack of the most highly active •OH radicals results in the biological toxicity of the systems after the reactions considerably high; additionally, water matrix such as co-existed ions and dissolved organic matter (DOM) in practical wastewater will greatly affect the degradation efficiency of organic micropollutants. It is still a critical challenge to realize the deep oxidation of recalcitrant organic micropollutants in wastewater to less toxic or nontoxic products by single photocatalysis or Fenton process. In this regard, coupling of

photocatalysis with heterogeneous Fenton-like process to establish the robust heterogeneous photo-Fenton-like catalytic oxidation process brings a bright prospect in the remediation of recalcitrant organic micropollutants from wastewater since more plentiful •OH radicals are generated, benefiting from the accelerated ≡Fe(III) to ≡Fe(II) regeneration dynamics and thus the improved H_2O_2 activation efficiency, assisted by the injection of photogenerated electrons to the Fenton-like process. In this hot research topic, designing robust heterogeneous photo-Fenton-like catalysts and understanding the reaction mechanism of photo-Fenton-like catalytic oxidation processes are the key scientific issues [4,5].

More recently, the increased interests are focusing on the development of semiconductor photocatalyst-based transition metal (e.g., Fe, Mn, Cr, Co or Cu) single atom catalysts (SACs) for heterogeneous photo-Fenton-like applications [6–12]. By combination of the advantages of well-defined active sites, maximum transition metal atom utilization efficiency, homogeneously dispersed transition metal sites throughout the photocatalyst supports at the atomic level, unique electronic structure and strong transition metal site-photocatalyst interactions, the photocatalyst-based transition metal SACs exhibit significantly enhanced photo-Fenton-like oxidation activity in the deep oxidation of

---

* Corresponding authors.
E-mail addresses: yangyx374@nenu.edu.cn (Y. Yang), guoyh@nenu.edu.cn (Y. Guo).

organic micropollutants; furthermore, the strong transition metal site-photocatalyst interactions are expected to inhibit transition metal leaching to not only avoid secondary pollution but also ensure long-term catalytic stability. This active research area is appealing wide attentions in environmental catalysis [13]. Among various prevalent photocatalysts such as TiO_2, Bi-based compounds and graphitic carbon nitride (g-C_3N_4), π-conjugated polymeric g-C_3N_4 shows especial superiority for anchoring transition metal sites to fabricate g-C_3N_4-based transition metal SACs. Polymeric g-C_3N_4 has intrinsic advantages of visible-light response and strong light harvesting capacity; moreover, g-C_3N_4 shows flexible molecular structure, which renders it easily adjustable electronic structures and band structures through versatile molecular engineering strategies; particularly, sp^2-hybridized N atoms in "six-fold-cavities" of g-C_3N_4 framework offer multidentate coordination sites to chemically stabilize and homogeneously disperse the isolated transition metal atoms by donating the lone pairs of electrons to empty *d* orbital of transition metal to form M−N coordination bonding. Nevertheless, bulk g-C_3N_4 still faces two drawbacks for the fabrication of efficient g-C_3N_4-based Fe SACs. On the one hand, delocalized distribution of electrons on LUMO and holes on HOMO endows g-C_3N_4 sluggish separation and transfer dynamics of the photoexcited charges and thus poor utilization efficiency of the photoexcited electrons; additionally, ionic radius of the transition metal for the constructed Fenton catalysts is relatively small (e.g., Fe^{3+} 0.79 Å), and the coordination interaction between Fe atom and sp^2-hybridized N atom is weak, which is unfavorable to firmly stabilize Fe single atoms (SAs) because of weak orbital overlapping or hybridization.

To overcome these obstacles and fabricate advanced g-C_3N_4-based Fe SAs photo-Fenton-like catalysts, the present work develops an *in-situ* route to prepare C-rich g-C_3N_4 (C-CN) embedded interlayer Fe−N_4 single-atom sites catalyst (Fe$_1$/C-CN), and the process includes a supramolecule self-assembly of melamine (MA) with cyanuric acid (CA) in the presence of glucose (Glu) and Fe(NO_3)$_3$ to hydrogen bonded supramolecular aggregate (Fe/Glu-MCS) followed by thermal polymerization. During this process, glucose plays a pivotal role. Specifically, certain graphitic carbon rings (C$_{ring}$) with sp^2-hybridized π-conjugated bonding derived from thermal polymerization of Fe/Glu-MCS are introduced to heptazine framework of g-C_3N_4, leading to modifying electronic structure and increasing electronic densities around sp^2-hybridized N atoms [14]. Accordingly, orbital hybridization between N 2p and Fe 3d is reinforced, facilitating the formation of strong Fe−N coordination bonds for not only stabilizing Fe species to Fe SAs on C-CN but also further boosting charge separation and transfer dynamics by directly delivering photogenerated electrons to Fe SAs and thus accelerating the regeneration of ≡Fe(II); additionally, the adjacent hydroxyl groups on glucose molecules can chelate Fe^{3+} to glucose-chelated Fe^{3+} in Fe/Glu-MCS, so that the agglomeration of Fe species to Fe clusters is restrained during subsequent thermal polymerization process. The above route can also lead to Fe$_1$/C-CN porous ultrathin sheet-like nanostructure, which is favorable for the physical confinement of Fe species to Fe SAs [15]. By combination of multiple advanced characterizations and DFT calculations, well-defined structure of Fe$_1$/C-CN is proposed, in which interlayer Fe−N_4 coordination configuration is established.

The Fe$_1$/C-CN exhibits remarkably high photo-Fenton-like catalytic oxidation activity toward two visible-light-insensitive and recalcitrant organic micropollutants, *p*-nitrophenol (PNP) and methylparaben (MPB), in a wide pH window (2.9−7.5) and the presence of DOM, outperforming its photocatalytic activity and heterogeneous Fenton-like activity. Furthermore, the Fe$_1$/C-CN photo-Fenton-like catalyst is also robust in the treatment of pharmaceutical wastewater containing six mixed emerging organic micropollutants, including levofloxacin (LEV), tenormine (TEN), atrazine (ATN), acetaminophen (APAP), MPB and PNP, and all the recalcitrant organic micropollutants can be decontaminated rapidly and completely with a high mineralization efficiency. More importantly, the catalytic activity loss of Fe$_1$/C-CN is negligible

after five times' catalytic cycles; meanwhile, leaching of Fe species and the agglomeration of Fe SAs hardly occur, originating from the strong interlayer Fe−N coordination interactions. This outstanding deep oxidation capacity and robust durability in the long-term remediation of organic micropollutants make Fe$_1$/C-CN photo-Fenton-like catalyst great prospects for sustainable and resource-saving environmental remediation. Combination of experimental results and DFT calculations, incisive insights are provided to understand the structure-activity relationships and catalytic reaction mechanism of Fe$_1$/C-CN photo-Fenton-like system at the atomic scale, revealing that anchoring Fe SAs can introduce abundant and highly catalytic active sites and thus the maximum Fe atom utilization; simultaneously, as-built interlayer Fe−N coordination bonding creates a novel and atomic-scale interlayer electron transfer channel to direct electron migration efficiently, which leads to the yield of long-lived free photogenerated electrons and holes at the surface of Fe$_1$/C-CN. As a consequence, the redox cycle of ≡Fe(III) ↔ ≡Fe(II) is triggered, accompanying with the notably improved H_2O_2 activation efficiency. Plentiful •OH radicals yielded from both Fe$_1$/C-CN photocatalysis and photo-Fenton-like catalysis processes together with superoxide radical (•O_2^-) and singlet oxygen ($^1O_2$) generated from Fe$_1$/C-CN photocatalysis process ensure Fe$_1$/C-CN photo-Fenton-like catalyst deep oxidation capacity towards recalcitrant organic micropollutants.

2. Experimental

2.1. Catalyst Preparation

Carbon-rich g-C_3N_4 embedded interlayer Fe−N_4 single-atom sites catalyst (Fe$_1$/C-CN) was prepared as follows. Melamine (MA, 3 g) and glucose (Glu, 30 mg) were dispersed to ethanol (30 mL) to obtain suspension A. Simultaneously, cyanuric acid (CA, 3 g) and Fe(NO_3)$_3$•9H_2O (10 mg) were dispersed to ethanol (30 mL) to obtain suspension B. Both suspensions were continuously stirred for 12 h, and then suspension B was added to suspension A under stirring for 20 min. The mixture was hydrothermally treated at 180 °C for 12 h. After the reaction, the yielded brownish-red precipitate was filtrated and then washed with deionized water until the effluent reached neutrality. After being dried at 80 °C for 12 h, MA-CA-glucose-chelated Fe supramolecular aggregated (Fe/Glu-MCS) was obtained. The Fe/Glu-MCS was then calcined at 550 °C for 2 h with a heating ramp of 2.5 °C min^{-1} under a nitrogen gas flow to Fe$_1$/C-CN. In the above system, initial molar ratio of MA-to-CA-to-Glu is 0.979:1:0.007. For comparison, carbon-rich g-C_3N_4 (C-CN), g-C_3N_4 embedded Fe species (Fe/CN) and g-C_3N_4 (CN) were respectively prepared by using the above method in the absence of Fe(NO_3)$_3$•9H_2O, glucose, and both Fe(NO_3)$_3$•9H_2O and glucose. Fe doping level in Fe/CN and Fe$_1$/C-CN was 0.16 wt%, determined by a Perkin-Elmer Avio 200 ICP-MS.

2.2. Heterogeneous photo-Fenton-like degradation of organic micropollutant tests

The tests were carried out at natural pH (pH = 7.5) and room temperature. In a typical test, 50 mg of catalyst powder was added to 50 mL of PNP or MPB solution (c_0 = 10 mg L^{-1}). The suspension was ultrasonicated for 5 min to guarantee a homogeneous dispersion and then stirred for 60 min in dark to establish adsorption-desorption equilibrium between the target pollutant and the catalyst. The reaction was initiated by adding 250 μL of H_2O_2 aqueous solution (30%) and light irradiation supplied by a PLS-SXE300 Xe lamp (300 W) with IR and 400 nm cutoff filters. At regular light irradiation time intervals, 1 mL of suspension was taken out and filtrated by a 0.22 μm filter for the determination of the concentration of PNP and MPB by an Agilent 1260 HPLC liquid chromatograph equipped with a C18 column and UV detector. The HPLC determination conditions of each organic micropollutant are listed in Table S1.

Detailed information regarding catalyst characterization (Text S1),

pollutant determination method (Text S2), optical parameters evaluation (Text S3), photoelectrochemical measurements (Text S4), and theoretical calculations (Text S5) are provided in Supplementary material.

3. Results and discussion

3.1. Fabrication and characterization of C-rich g-C_3N_4 embedded interlayer Fe−N_4 single-atom sites catalyst

Strong coordination bonding between sp^2-hybridized N atoms in g-C_3N_4 with Fe species is a prerequisite for the stabilization of isolated Fe atoms on g-C_3N_4 supports. For this purpose, an *in-situ* strategy of supramolecule self-assembly of MA with CA in the presence of glucose and Fe(NO$_3$)$_3$ followed by thermal polymerization is designed to ensure not only the incorporation of graphitic C$_{ring}$ to heptazine units but also the chelation with Fe to stabilize Fe SAs. As illustrated in Fig. 1a, mixing MA and glucose in ethanol under room temperature produces N−H•••O bonded MA-Glu. After mixing MA-Glu with the mixture of CA and Fe^{3+}, MA-Glu and CA self-assemble to N−H•••O and N−H•••N bonded Glu-MCS aggregate; meanwhile, the adjacent hydroxyl groups on glucose molecules rapidly chelate Fe^{3+} to form glucose-chelated Fe/Glu-MCS aggregate. The formation of Fe/Glu-MCS aggregate ensures anchoring the isolated Fe sites on C$_{ring}$-incorporated g-C_3N_4 (C-CN) from agglomeration during subsequent hydrothermal treatment (HT, 180 °C) and thermal polymerization (550 °C) processes [16]. The HT process can further fasten the Fe/Glu-MCS framework and facilitate the interactions among various components. After thermal polymerization of the Fe/Glu-MCS, MCS polymerizes to a heptazine-based g-C_3N_4 framework; meanwhile, glucose polymerizes to graphitic C$_{ring}$ with sp^2-hybridized π-conjugated bonding, and these C$_{ring}$ units are incorporated to heptazine units by the replacement of certain triazine units to yield C-rich g-C_3N_4. The above thermal polymerization process also accompanies the breakage of Fe−O bond in Fe/Glu-MCS and the establishment of Fe−N coordination bonding to produce Fe$_1$/C-CN catalyst. Because the electronegativity of C atom is lower than that of N atom, graphitic C$_{ring}$ as an electron donor in C-CN can donate electrons to triazine ring (as an electron acceptor), which gives rise to the increased electron density around sp^2-hybridized N atom in C-CN framework. Therefore, orbital overlap between N $2p$ and Fe $3d$ is strengthened, leading to the formation of strong Fe−N coordination bonding for tightly anchoring and homogeneously dispersing the isolated Fe SAs on C-CN.

Furthermore, during the processes of HT and subsequent thermal polymerization of Fe/Glu-MCS to sheet-like Fe$_1$/C-CN, the released H$_2$O, CO$_2$ and NH$_3$ gases not only sufficiently exfoliate the sheets of Fe$_1$/C-CN to ultrathin nanosheets but also etch the nanosheets to create abundant pores on the Fe$_1$/C-CN nanosheets. This unique morphological characteristic provides a physical confinement space for Fe species to the isolated atoms. Therefore, Fe SAs are firmly and homogeneously anchored on C-CN support by combination of strong Fe−N coordination bonding and physical confinement of porous ultrathin C-CN nanosheets.

To reveal the morphological characteristics and porosity properties of Fe$_1$/C-CN heterojunctions as well as the coordination environment of Fe SAs in Fe$_1$/C-CN, the following powerful characterization techniques combined with DFT calculations are conducted.

Firstly, the morphological characteristics of Fe$_1$/C-CN are observed by a high-resolution transmission electron microscope (HRTEM), and the reference samples including g-C_3N_4 (CN), C-CN and g-C_3N_4 embedded Fe species (Fe/CN) are also tested. As displayed in Fig. 1b, CN exhibits sheet-like nanostructures with randomly distributed pores on the sheets. In comparison of CN, C-CN nanosheets tend to curl, suggesting that a small amount of glucose added in the preparation system has some influence on the morphology of C-CN nanosheets (Fig. 1c). Fe/CN and Fe$_1$/C-CN display a similar morphology with that of their CN and C-CN supports; moreover, Fe species are hardly observed in HRTEM images (Fig. 1d and e). Nevertheless, the high-angle annular dark field

scanning transmission electron microscopy (HAADF-STEM) test can provide unambiguous evidence to confirm the formation of atomically dispersed Fe on Fe$_1$/C-CN nanosheets, highlighted by the well-distributed bright dots with a diameter of 0.3 nm in the image (Fig. 1f). Additionally, HAADF-STEM element mapping images shown in Fig. 1g indicate that Fe, C and N elements homogeneously disperse throughout Fe$_1$/C-CN nanosheets. As for Fe/CN prepared in the absence of glucose, single Fe atoms are hardly observed from its HAADF-STEM image (Fig. S1); however, Fe, C and N elements in Fe/CN nanosheets show homogeneous dispersion. The above result reflects the crucial role of glucose in facilitating the formation of atomically dispersed Fe on C-CN. By atomic force microscopy (AFM) measuring, the average thickness of C-CN and Fe$_1$/C-CN nanosheets is 3.2 and 3.7 nm, respectively (Fig. 1h and i, as well as Fig. S2).

The BET surface areas and pore volumes of Fe$_1$/C-CN and the reference samples are calculated from the determined nitrogen gas sorption isotherms (Fig. S3), and the results are summarized in Table S2. C-CN possesses much larger BET surface area (118.1 m^2 g^{-1}) and pore volume (0.70 cm^3 g^{-1}) than CN (69.6 m^2 g^{-1} and 0.40 cm^3 g^{-1}), consistent with its curled and thin sheet-like nanostructures and thus more plentiful aggregate pores on the sheets. Similarly, the BET surface area and pore volume of Fe$_1$/C-CN (94.4 m^2 g^{-1} and 0.57 cm^3 g^{-1}) are larger than Fe/CN (79.3 m^2 g^{-1} and 0.42 cm^3 g^{-1}). The appealing porosity properties of Fe$_1$/C-CN can provide more exposed active sites, improve light harvesting ability and promote photoinduced charge separation and transfer process.

CHN elemental analysis results indicate that C-CN (0.592) shows slightly higher C-to-N molar ratio than CN (0.576), in line with the incorporation of certain C$_{ring}$ to heptazine framework. Additionally, the appearance of characteristic diffraction peaks at 10.8, 11.9, 22.1, 28.1 and 33.2° in the X-ray diffraction (XRD) patterns confirms the formation of supramolecular aggregates in both MCS and Fe/Glu-MCS samples (Fig. S4a and JCPDS file 05–0127) [17], while the identified diffraction peaks at 13.1° (100) and 27.5° (002) that corresponds to the in-plane structural repetitive heptazine units and interplanar stacking of aromatic C−N heterocycles suggest a primary graphite-like layered structure of g-C_3N_4 maintains intact after the incorporation of certain C$_{ring}$, Fe species, or both C$_{ring}$ and Fe species to g-C_3N_4 framework (Fig. S4b). According to Bragg equation, the interlayer distance of g-C_3N_4 (0.32 nm) is calculated [18]. Fourier transform infrared (FT-IR) spectra demonstrate that CN, C-CN, Fe/CN and Fe$_1$/C-CN all show three types of characteristic vibrational absorption peaks including a sharp peak at 817 cm^{-1}, a group of weak peaks in the range of 1200−1700 cm^{-1} and a broad peak at 2800−3500 cm^{-1} (Fig. S4c), and they are assigned to the bending vibrations of heptazine units, stretching vibrations of aromatic C−N heterocycles and terminal −NH/NH$_2$ groups, respectively [19]. The result confirms that the primary chemical structure of g-C_3N_4 remains intact after the incorporation of certain C$_{ring}$, Fe species, or both C$_{ring}$ and Fe species to g-C_3N_4 framework.

Electron spin resonance (ESR) analysis provides a basic understanding of changes in electronic structure of g-C_3N_4 after the incorporation of C$_{ring}$ or the incorporation of C$_{ring}$ and the formation of Fe−N coordination bonds. As shown in Fig. S4d, CN exhibits a weak intensity of Lorentzian line at $g = 2.003$, originating from a few unpaired and/or delocalized electrons in aromatic C−N heterocycles [20]. In the cases of C-CN and Fe$_1$/C-CN, their Lorentzian lines also emerge at $g = 2.003$, together with the increased signal intensity than CN; moreover, C-CN shows stronger Lorentzian line signal than Fe$_1$/C-CN. This increased signal intensity suggests the generation of more abundant delocalized electrons in aromatic C−N heterocycles of C-CN or Fe$_1$/C-CN because of the introduction of π-electron-rich C$_{ring}$ [21,22], in addition, the decreased Lorentzian line signal intensity of Fe$_1$/C-CN is caused by the decrease of the number of the delocalized electrons because some delocalized electrons from aromatic C−N heterocycles have donated to empty d orbitals of Fe species.

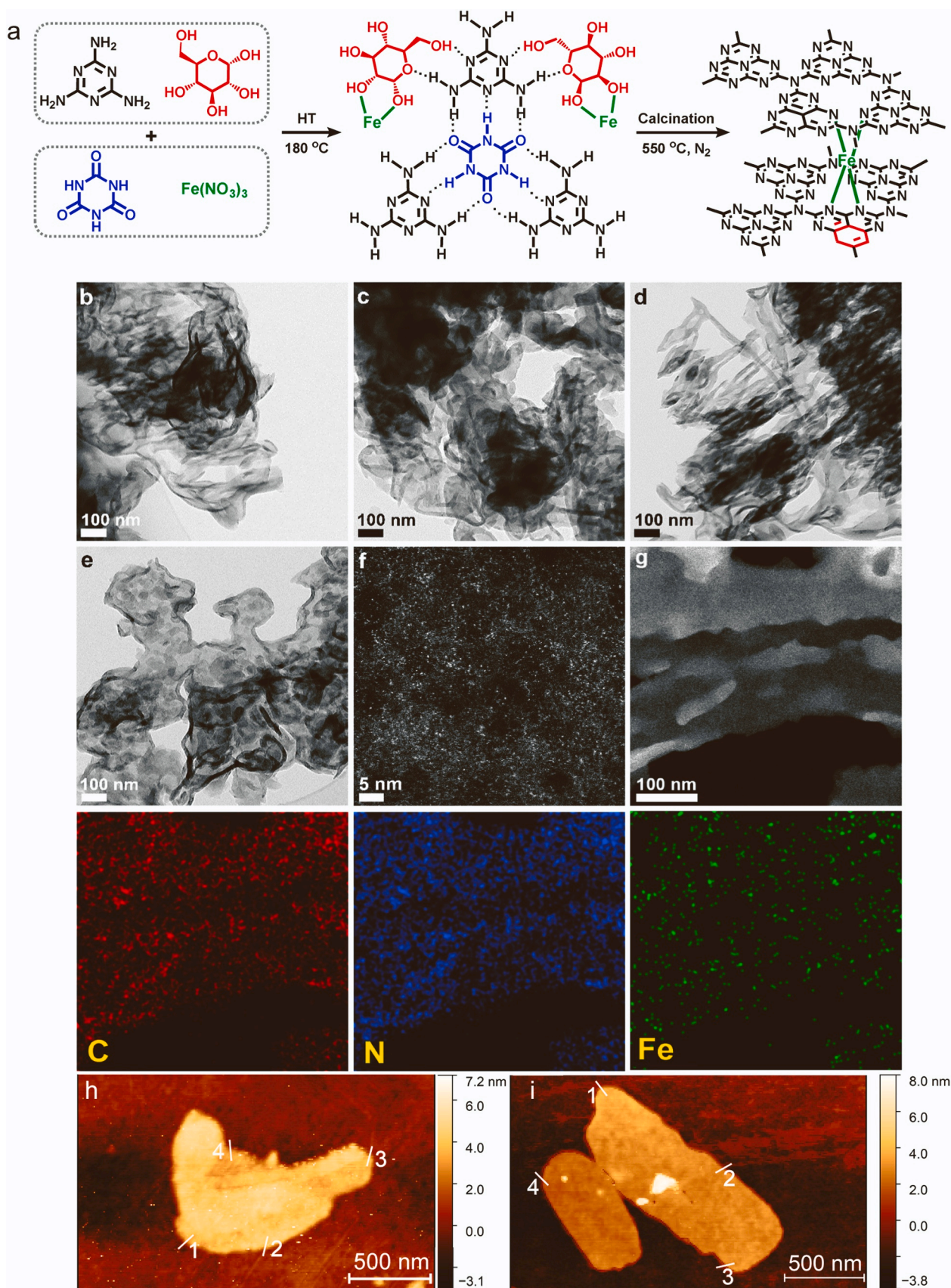The coordination environment of Fe SAs and the position of the

Fig. 1. (a) Schematic illustration of the preparation route and framework structure of Fe$_1$/C-CN. HRTEM images of (b) CN, (c) C-CN, (d) Fe/CN and (e) Fe$_1$/C-CN. (f) HAADF-STEM images and (g) the representative element mapping images of Fe$_1$/C-CN. AFM images of (h) C-CN and (i) Fe$_1$/C-CN.

doped C_{ring} units in C-CN support are studied by X-ray photoelectron spectroscopy (XPS), X-ray absorption spectroscopy (XAS) and DFT calculations. As shown in Fig. 2a, C 1s XPS spectrum of CN exhibits two prominent binding energy (BE) peaks at 284.6 and 288.2 eV, attributing to the C−C bonds from adventitious C species and N−C=N coordinations in the skeleton of g-C$_3$N$_4$, respectively [23]. As for C-CN, the

above two BE peaks still are visibly observed, but the N−C=N/C−C=C coordinations of C-CN shifts to a lower BE region (288.0 eV) compared to CN, consistent with the incorporation of certain graphitic C_{ring} to heptazine framework. Graphitic C_{ring} have more plentiful π-electrons, and the electron donation from graphitic C_{ring} to N−C=N coordinations renders a slight increase in electron density of N−C=N coordinations
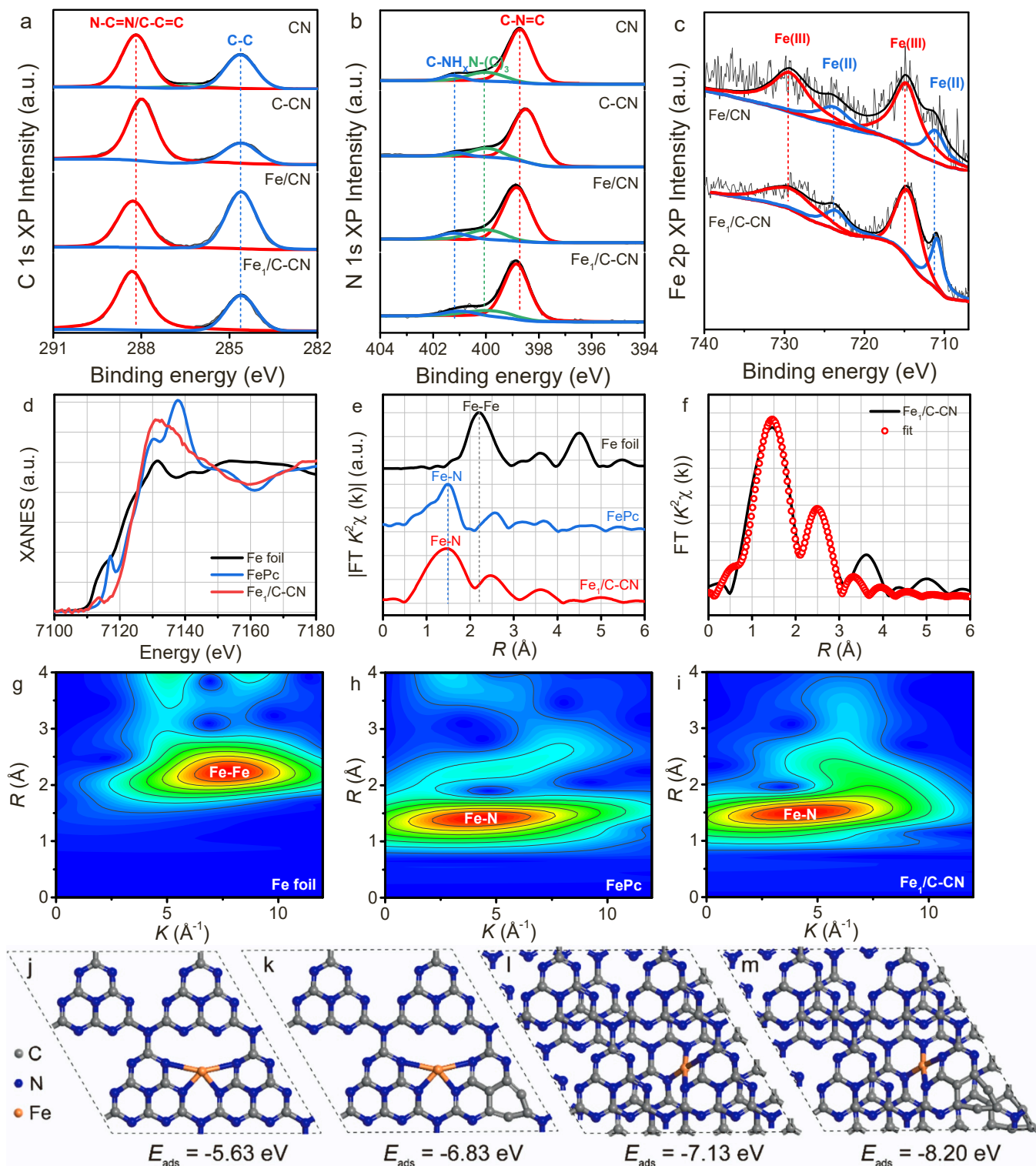

Fig. 2. XPS spectra of g-C$_3$N$_4$-based materials in the (a) C 1s, (b) N 1s and (c) Fe 2p binding energy regions. (d) Normalized Fe K-edge XANES spectra and (e) k^2-weighted Fe K-edge FT-EXAFS spectra at R space of Fe$_1$/C-CN and reference samples. (f) The k^2-weighted Fe K-edge EXAFS fitting curve of Fe$_1$/C-CN at R space. Wavelet transform of (g) Fe foil, (h) FePc and (i) Fe$_1$/C-CN. The possible coordination approaches of Fe atoms on (j, l) CN and (k, m) C-CN as well as the corresponding E_{ads} values of Fe atoms at different anchoring sites.

and thereby somewhat declined BE value [24]. Regarding to Fe/CN and Fe₁/C-CN samples, their N−C=N coordination peaks shift to higher BE value (288.3 eV) in comparison of CN and C-CN, highlighting a decrease in the electron density of N−C=N coordinations in some extent. The result is caused by the formation of Fe−N coordination bonding in Fe/CN and Fe₁/C-CN, in which sp^2-hybridized N atoms provide lone pairs of electrons to empty d orbit of Fe species, leading to the transfer of electrons from N to Fe atoms. Particularly, in comparison of Fe/CN, Fe₁/C-CN shows a higher BE value shift of N−C=N coordinations, implying the strengthened Fe−N coordination interactions. The result is caused by the increased electron density of N−C=N coordinations in C-CN, which reinforces the orbital hybridization between N $2p$ and Fe $3d$.

As shown in Fig. 2b, the N 1s XPS spectra of CN, C-CN, Fe/CN and Fe₁/C-CN all demonstrate three characteristic peaks centered at 398.5−399.0, 400.0 and 401.2 eV, respectively, and they are assigned to two-coordinated nitrogen (C–N=C or N_{2C}), three-coordinated nitrogen (N–(C)₃ or N_{3C}) and N atoms from unpolymerized –NH/–NH₂ group, respectively [25]. The shift of C–N=C coordinations to lower BE region from CN (398.7 eV) to C-CN (398.5 eV) suggests the increased electron density, which is also attributed to the incorporation of certain graphitic C_{ring} to heptazine framework. In the cases of Fe/CN and Fe₁/C-CN samples, their C−N=C BE peaks both shift to higher value (399.0 eV) in comparison of their corresponding supports; furthermore, Fe₁/C-CN shows more obvious shift of C−N=C BE peak (from 398.5 to 399.0 eV) with respect to Fe/CN (from 398.7 to 399.0 eV). The result further indicates the decreased electron density in C–N=C coordinations, originating from the electron donation from sp^2-hybridized N atoms in CN or C-CN to Fe $3d$ orbitals to form Fe−N coordination bond; additionally, the coordination ability between N and Fe atoms is reinforced after the incorporation of graphitic C_{ring} to heptazine framework because of the increased orbital overlap between N $2p$ and Fe $3d$, which provide a prerequisite for stabilizing isolated Fe atoms on C-CN support.

From Fe 2p XPS spectra shown in Fig. 2c it is found that Fe/CN exhibits four deconvoluted peaks positioned at 711.2 (Fe(II) $2p_{3/2}$), 723.7 (Fe(II) $2p_{1/2}$), 714.7 (Fe(III) $2p_{3/2}$) and 729.3 eV (Fe(III) $2p_{1/2}$), respectively, indicating the coexistence of ≡Fe(II) and ≡Fe(III) species [11]. In the case of Fe₁/C-CN, the above BE peaks are still identified but shift towards lower BE values for *ca.* 0.2 eV compared to Fe/CN, reflecting an increased electron density around Fe species in C-CN support, contributing from sp^2-hybridized N atoms in C-CN support. Additionally, higher peak intensity ratio of ≡Fe(II)-to-≡Fe(III) in Fe₁/C-CN (0.56) than Fe/CN (0.40) suggests that Fe₁/C-CN possess more ≡Fe(II)−N sites, which is beneficial to the heterogeneous photo-Fenton-like catalytic reactions.

Subsequently, in order to provide deep insight into the atomic oxidation state and coordination environment of Fe species in Fe₁/C-CN heterojunction, the authoritative synchrotron-based XAS technique is applied. Firstly, the atomic oxidation state-sensitive Fe K-edge X-ray absorption near-edge structure (XANES) spectra are tested to estimate the atomic oxidation state of Fe in Fe₁/C-CN. As shown in Fig. 2d, the absorption edge of Fe₁/C-CN shifts to higher energy level compared to that of Fe foil and is closer to the reference iron phthalocyanine (FePc). Therefore, the positively charged $Fe^{\delta+}$ is formed in Fe₁/C-CN [26]. Next, the average distance between Fe and N atoms and the coordination number of Fe atoms are interpreted by Fourier transform extended X-ray absorption fine structure (FT-EXAFS). As shown in Fig. 2e, the FT k^2-weighted Fe K-edge EXAFS curve of Fe₁/C-CN exhibits a prominent peak at 1.49 Å, in line with that of FePc and corresponding to bond length of Fe−N coordinations; additionally, compared with Fe foil, no Fe−Fe coordination peaks at 2.20 and 4.42 Å are observed in Fe₁/C-CN [26]. On the basis of the above XANES and FT-EXAFS analysis it is strongly suggested that atomically dispersed Fe are formed and stabilized on C-CN support by the established strong Fe−N coordination bonds. The Fe K-edge FT EXAFS fittings in R space (Fig. 2f) and k space (Fig. S5) are applied to obtain the quantitative structural parameters for

Fe₁/C-CN. The fitting results indicate that the coordination number of the central Fe atom bonding to adjacent N atoms is 4, corresponding to Fe−N₄ configuration in Fe₁/C-CN. The wavelet transform (WT) contour plots are employed to investigate the Fe K-edge EXAFS oscillations of Fe₁/C-CN and the references (Fig. 2g−i). The WT intensity maximums of Fe₁/C-CN locate at $R = 1.97$ Å and $k = 4.0$ Å⁻¹, and the values are close to those in the reference FePc ($R = 1.93$ Å and $k = 4.2$ Å⁻¹) but differ from the features of Fe foil ($R = 2.47$ Å and $k = 8$ Å⁻¹). The result further supports the above FT-EXAFS analysis.

According to Fe₁/C-CN preparation route and the above multiple structural characterization results, the possible in-plane and interlayer Fe−N₄ coordination configurations of Fe atoms on C-CN support are proposed and illustrated in Fig. 2k and m, and for comparison, the possible in-plane and interlayer Fe−N₄ coordination configurations of Fe atoms on CN support are also provided (Fig. 2j and l). Based on these configurations, the adsorption energy values (E_{ads}) of Fe atoms at different anchoring sites are calculated. As shown in Fig. 2j and k, for CN- and C-CN-embedded Fe species (Fe/CN and Fe₁/C-CN), they are confined in in-plane "six-fold-cavities", and the corresponding E_{ads} values are −5.63 and −6.83 eV, respectively. Higher E_{ads} value of Fe₁/C-CN than Fe/CN is caused by the increased electron density around sp^2-hybridized N atoms in C-CN support and thereby the reinforced orbital overlap between N $2p$ and Fe $3d$. In the cases of interlayer Fe−N₄ sites-embedded in CN (Fig. 2l) and C-CN (Fig. 2m), their E_{ads} values are −7.13 and −8.20 eV, respectively, higher than those of the in-plane Fe−N₄ sites-embedded in CN and C-CN. The result suggests that the interlayer Fe−N₄ coordination is the optimal configuration for Fe/CN or Fe₁/C-CN, and higher E_{ads} value of Fe₁/C-CN than Fe/CN further confirms the significance of graphitic C_{ring}-incorporation for modulating the electronic structure of g-C₃N₄ and thereby the coordination environment of Fe atoms.

Changes of the electronic structure of C-CN, Fe/CN or Fe₁/C-CN with respect to CN also reflect in their light absorption properties, which are characterized by ultraviolet-visible diffuse reflectance spectroscopy (UV–vis/DRS) method. As displayed in Fig. 3a, the tested samples including CN, C-CN, Fe/CN and Fe₁/C-CN exhibit the similar intrinsic light absorption in the range of 200−450 nm, attributing to π−π* electron transition of aromatic C−N heterocycles [27]; additionally, C-CN, Fe/CN and Fe₁/C-CN also exhibit a new and weak visible-light absorption (450−800 nm). For C-CN, its visible-light absorption is caused by the intramolecular charge transfer (IMCT) from graphitic C_{ring} to triazine rings. In the case of Fe/CN, its visible-light absorption originates from the intervalence charge transfer (IVCT) of Fe species [28]. As for Fe₁/C-CN, both IMCT and IVCT bands should exist, however, due to the atomically distributed Fe with a low loading level (0.16 wt%), the contribution from IVCT band of Fe SAs is overshadowed by IMCT band. Consequently, Fe₁/C-CN exhibits the same light absorption properties as those of C-CN. From the plots of the converted Kubelka−Munk function *vs.* photon energy (Fig. 3b), the estimated bandgap (E_g) values of various samples are very close, and they are 2.69 (CN), 2.67 (C-CN), 2.65 (Fe/CN) and 2.65 eV (Fe₁/C-CN), respectively. To determine the conduction band (CB) edge potentials (E_{CB}) of the samples, Mott-Schottky measurements are conducted under three different frequencies. By determining the intersections of tangent of Mott-Schottky plots with the x-axis, E_{CB} values are obtained (Fig. S6). Based on the determined E_{CB} and E_g values, the valence band (VB) edge potentials (E_{VB}) are calculated. Correspondingly, the energy band alignments of various g-C₃N₄-based samples are established (Fig. 3c).

The influence of the introduced C_{ring} units on the charge density spatial distribution of LUMO and HOMO of C-CN is calculated by DFT on the basis of the optimized structure models shown in Fig. 3d and g. For CN, its electrons on LUMO and holes on HOMO show delocalized distribution (Fig. 3e and f), which significantly impedes the separation and transfer of the charges due to the lack of driving force. In the case of C-CN, the electrons accumulate on C_{ring}-free heptazine units of LUMO, while the holes are predominantly on C_{ring}-contained heptazine units of
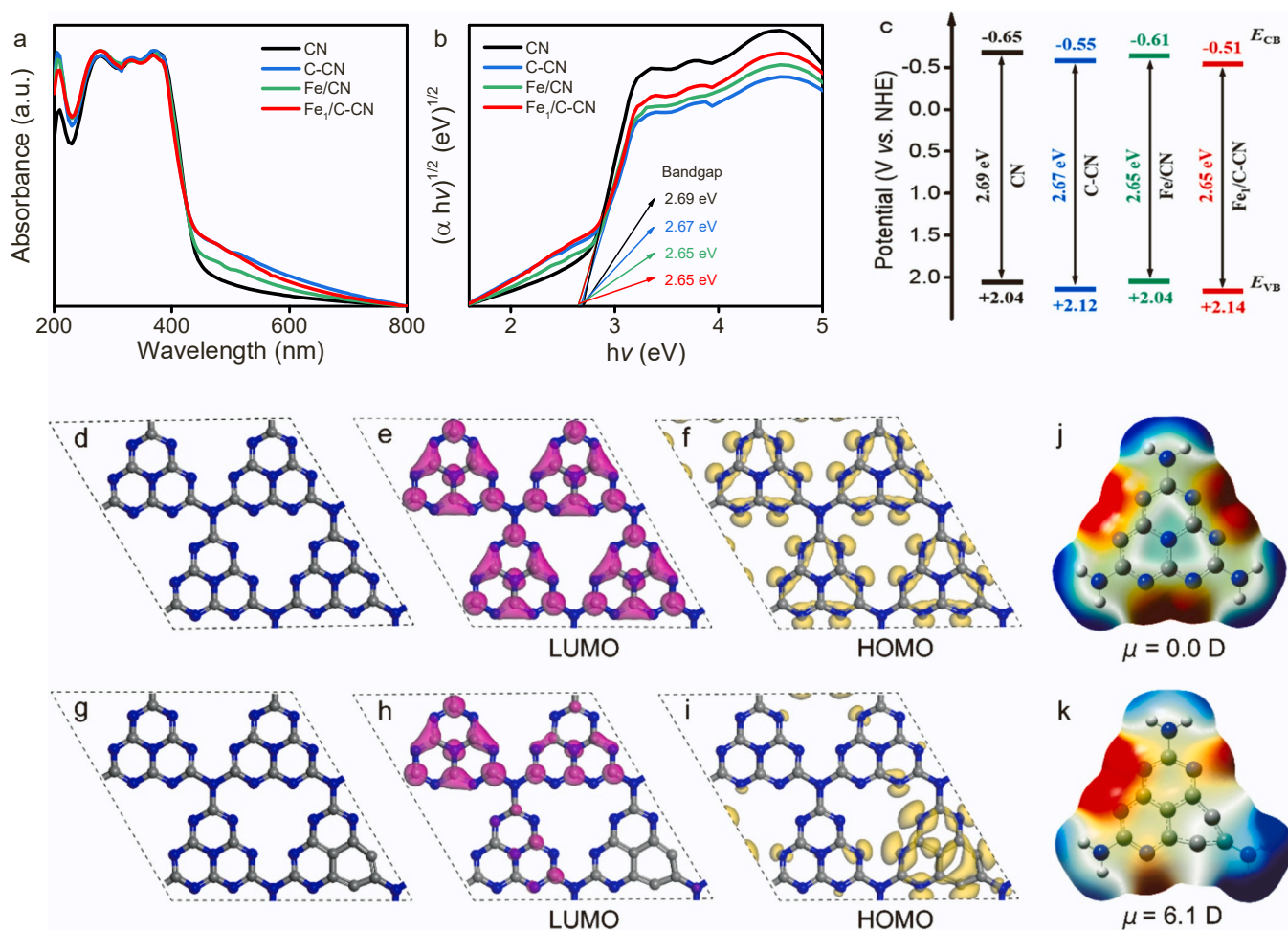
Fig. 3. (a) UV–vis/DRS, (b) the transformed Kubelka-Munk function *vs.* photon energy and (c) the energy band alignments of CN, C-CN, Fe/CN and Fe₁/C-CN. The optimized structure models of (d) CN and (g) C-CN, and the calculated charge density spatial distributions on LUMO and HOMO in (e, f) CN and (h, i) C-CN structures. Magenta and yellow colors represent the distributions of electrons in LUMO and holes in HOMO, respectively. ESP surface distribution and molecular dipole moments of (j) CN and (k) C-CN.

HOMO (Fig. 3h and i). Therefore, the introduction of C$_{ring}$ units disrupts the homogeneous distribution of charges in C-CN, which results in the localized charge density spatial distributions and thus providing a strong driving force for effective charge separation and transfer.

The calculated electrostatic potential (ESP) surface distributions can sustain the above result. As shown in Fig. 3j, CN exhibits evenly distributed charges on the heptazine units, in which the electron-rich regions locate around six sp^2-hybridized N atoms (red color regions) and the electron-deficient regions distribute around the other areas (blue color areas). In the case of C-CN, the charge distribution becomes uneven, in which the electron accumulation around some sp^2-hybridized N atoms is intensified; simultaneously, the electron-deficient regions locate near C$_{ring}$ units (Fig. 3k). This uneven charge distribution on C-CN induces an intense molecular dipole ($\mu = 6.1$ Debye, Fig. S7), corresponding to a local electric field to facilitate charge transfer in heptazine structure.

3.2. Evaluation of heterogeneous photo-Fenton-like catalytic oxidation performance

The heterogeneous photo-Fenton-like catalytic oxidation performance of Fe₁/C-CN is firstly evaluated by the degradation and mineralization of two light-insensitive and recalcitrant organic micropollutants, PNP and MPB. PNP is widely used in pharmaceutical industry, petrochemical and explosive production as well as leather treatment [29], while MPB as an antimicrobial preservative mainly applies in the production of cosmetics and other personal care products, food and pharmaceuticals [30]. Both aromatic micropollutants display estrogenic activity in biotic communities, and they are frequently detected in aquatic environments [31,32].

The blank tests show that the degradation of PNP (Fig. 4a and b) and MPB (Fig. 4d and e) is not readily achievable by direct photolysis; additionally, all tested catalysts show poor adsorption capacities to PNP or MPB (less than 5.0%) after reaching the adsorption-desorption equilibrium. In photocatalysis process, Fe₁/C-CN displays a higher PNP or MPB removal efficiency than CN, C-CN and Fe/CN, indicating that both C$_{ring}$ unit introduction and Fe doping can facilitate the photocatalytic oxidation process of PNP or MPB. Additionally, in Fe₁/C-CN Fenton-like system (50 mmol L^{-1} H₂O₂), the removal efficiency of PNP or MPB is very low. Nevertheless, significant degradation of PNP or MPB is found in bulk g-C₃N₄-embedded Fe sites (Fe/CN) and C-rich g-C₃N₄-embedded interlayer single-atomic Fe−N₄ sites (Fe₁/C-CN) photo-Fenton-like systems; moreover, Fe₁/C-CN exhibits superior photo-Fenton-like catalytic oxidation activity to Fe/CN. The result highlights that the efficient H₂O₂ activation assisted by visible-light irradiated Fe₁/C-CN can notably facilitate the catalytic oxidation process of PNP or MPB; importantly, interlayer single-atomic Fe−N₄ sites with the advantages of the maximum Fe atom utilization efficiency and unique electronic structure play a dominated role to the significantly enhanced removal efficiency of two recalcitrant target organic micropollutants.
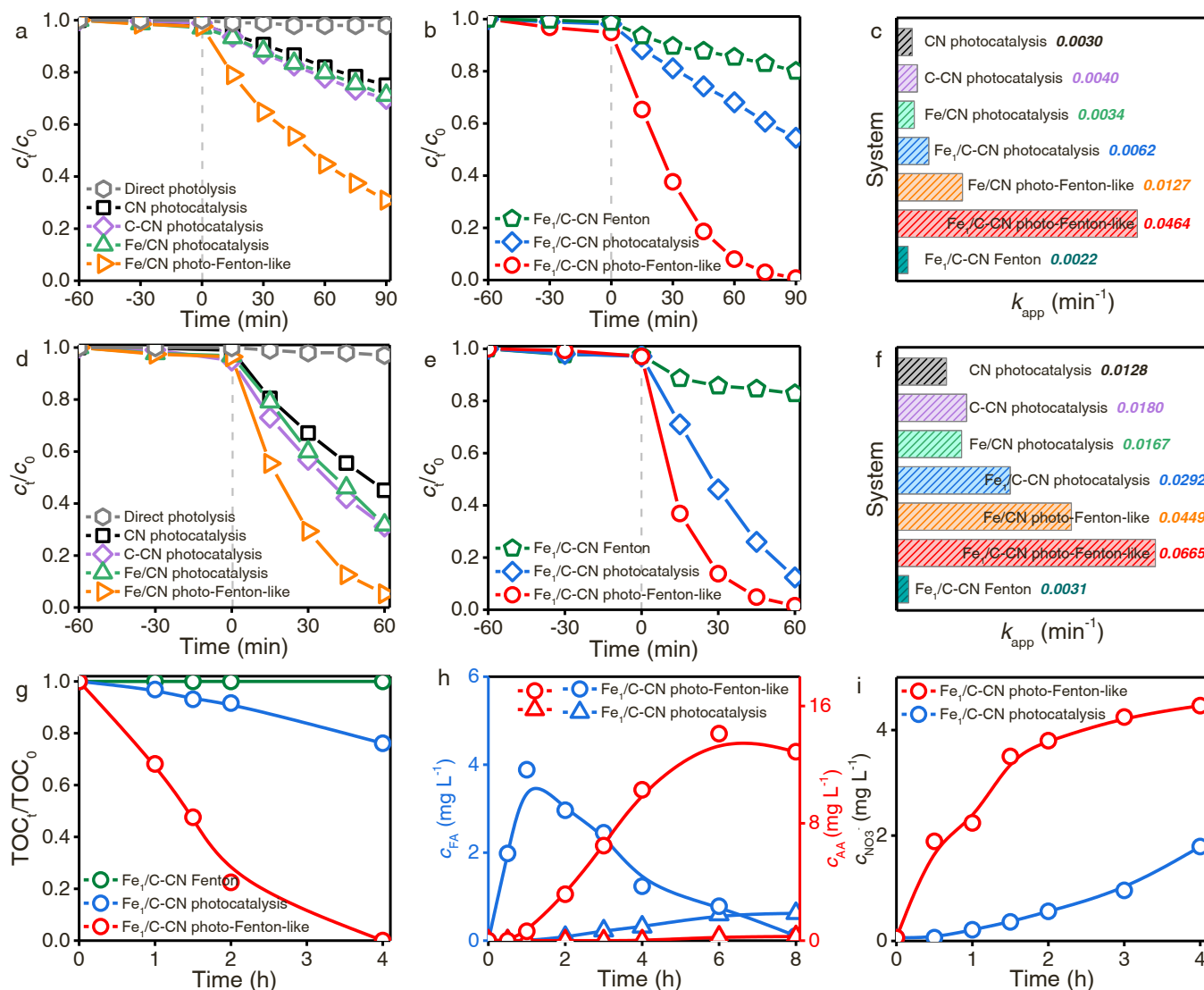
Fig. 4. The degradation curves of (a, b) PNP and (d, e) MPB in different systems and (c, f) the corresponding apparent kinetic rate constant. Catalyst amount 50 mg; c_0 (PNP or MPB) = 10 mg L^{-1}; volume 50 mL; $c_{(H2O2)}$ = 50 mmol L^{-1}; λ > 400 nm, pH = 7.5. Changes of (g) TOC values and (i) NO$_3^-$ concentrations during Fe$_1$/C-CN-assisted photo-Fenton-like degradation of PNP process. Catalyst amount 100 mg; c_0 (PNP) = 10 mg L^{-1}; volume 100 mL; $c_{(H2O2)}$ = 50 mmol L^{-1}; λ > 400 nm. (h) Concentration changes of formic acid and acetic acid during Fe$_1$/C-CN-assisted photo-Fenton-like degradation of PNP process. Catalyst amount 100 mg; c_0 (PNP) = 20 mg L^{-1}; volume 100 mL; $c_{(H2O2)}$ = 50 mmol L^{-1}; λ > 400 nm.

For example, over period of 90 min, the removal efficiency of PNP reaches up to 24.9 (CN photocatalysis), 30.2 (C-CN photocatalysis), 28.8 (Fe/CN photocatalysis), 69.1 (Fe/CN photo-Fenton-like), 19.9 (Fe$_1$/C-CN Fenton-like), 45.5 (Fe$_1$/C-CN photocatalysis) and 99.3% (Fe$_1$/C-CN photo-Fenton-like), respectively (Fig. 4a and b); additionally, after the reaction proceeds for 45 min, the removal efficiency of MPB reaches up to 44.4 (CN photocatalysis), 57.9 (C-CN photocatalysis), 53.9 (Fe/CN photocatalysis), 87.4 (Fe/CN photo-Fenton-like), 15.4 (Fe$_1$/C-CN Fenton-like), 74.0 (Fe$_1$/C-CN photocatalysis) and 95.1% (Fe$_1$/C-CN photo-Fenton-like), respectively (Fig. 4d and e).

The reaction kinetic plots ($-\ln c_t/c_0$ *vs.* t) of the degradation of PNP (Fig. S8a) and MPB (Fig. S8b) in the above various reaction systems show that the degradation processes conform well to pseudo-first-order kinetics, and thus the corresponding pseudo-first-order kinetic constants (k_{app}) are calculated. As shown in Fig. 4c, for PNP degradation, the k_{app} value of the most active Fe$_1$/C-CN photo-Fenton-like system (0.0464 min^{-1}) is 3.7 times higher than the Fe/CN photo-Fenton-like system (0.0127 min^{-1}), and 7.5 and 21.1 times higher than the Fe$_1$/C-CN photocatalysis (0.0062 min^{-1}) and Fe$_1$/C-CN Fenton-like

(0.0022 min^{-1}) systems, respectively. For MPB degradation, the k_{app} value of Fe$_1$/C-CN photo-Fenton-like system (0.0665 min^{-1}) is 1.5 times higher than the Fe/CN photo-Fenton-like system (0.0449 min^{-1}), and 2.3 and 21.5 times higher than the Fe$_1$/C-CN photocatalysis (0.0292 min^{-1}) and Fe$_1$/C-CN Fenton-like systems (0.0031 min^{-1}), respectively (Fig. 4f). Additionally, in comparison of photo-Fenton-like catalytic oxidation activity in the degradation of PNP reported recently in the typical photo-Fenton-like catalytic systems, the activity of Fe$_1$/C-CN still is comparable to or surpasses that of these systems (Table S3).

The rate of photon absorption in the reactor is one of the critical factors affecting the photocatalytic and photo-Fenton-like catalytic oxidation activity of CN, C-CN, Fe/CN and Fe$_1$/C-CN, while the rate of photon absorption in the reactor is closely related to the reactor optical thickness (τ) [33,34]. It is necessary to perform the catalytic tests of different catalysts at the same reactor optical thickness. According to the evaluation methods [35–38], the optical parameters, including spectral-averaged specific extinction coefficient (β^*), absorption coefficient (κ^*) and scattering coefficient (σ^*), of the above four catalysts

are calculated by converting the absorbances of catalyst suspension in transmittance and diffuse reflectance measurements (Text S3 and Fig. S9a and b), and the values for each catalyst are listed in Table S4. As an essential optical parameter closely related to the τ, the β^* value of CN, C-CN, Fe/CN and Fe$_1$/C-CN suspensions are 265, 343, 307 and 341 m^2 kg^{-1}, respectively. In current work, the photocatalytic and photo-Fenton-like catalytic oxidation reactions were carried out in a custom-designed cylindrical quartz reactor with a cross-section area ($S_{reactor}$) of 37.39 cm^2 (Fig. S9c). The visible-light irradiance (I_0) at the surface of the reaction liquid is 790 W m^{-2}. The catalyst mass concentration (C_m) was 1 mg mL^{-1}, and the depth of a 50 mL suspension in the reactor (x) was 0.015 m. According to Eqs. 1 and 2.

$$\tau = \beta^* C_m x \tag{1}$$

$$VRPA = S_{reactor} \int_0^x \beta^* C_m I_0 10^{-\beta^* C_m x} dx \tag{2}$$

τ values and volumetric rate of photon absorption (VRPA) values are calculated. As summarized in Table S4, the τ and VRPA values are 4.0 and 13.22 (CN), 5.2 and 13.34 (C-CN), 4.6 and 13.29 (Fe/CN), and 5.1 and 13.34 kW (Fe$_1$/C-CN), respectively. According to the literature work [36], the optimal range of τ value was 1.8–4.4. In four tested catalysts, only CN with τ value of 4.0 is in this optimum range. In order to evaluate the photocatalytic and/or photo-Fenton-like catalytic oxidation activity at the optimum range, the τ value of each catalyst suspension was set at 4.0 (consistent with CN). At τ value of 4.0, the concentrations of CN, C-CN, Fe/CN and Fe$_1$/C-CN were set again, and they are 1.00, 0.78, 0.87 and 0.78 mg mL^{-1}, respectively. As shown in Fig. S9d, at the same optical thickness of 4.0, Fe$_1$/C-CN still shows the optimal photocatalytic and/or photo-Fenton-like catalytic oxidation activity in the degradation of PNP among the tested catalysts, highlighting the superior photocatalytic or photo-Fenton-like catalytic oxidation performance of as-prepared interlayer single-atomic Fe−N$_4$ sites on C-CN.

The mineralization or deep oxidation ability is one of the most important performances of Fe$_1$/C-CN photo-Fenton-like catalyst, and therefore its mineralization ability is evaluated by the combined methods of monitoring the changes of total organic carbon (TOC) values, the concentration changes of the generated small molecular organic acid intermediates and NO$_3^-$ anion during the degradation process of PNP. For comparison, the mineralization ability of Fe$_1$/C-CN photocatalysis and Fenton-like catalysis are also tested. As shown in Fig. 4g, the TOC value of PNP/Fe$_1$/C-CN photo-Fenton-like system decreases sharply as the reaction goes on, and the removal efficiency of TOC reaches up to 100% after the reaction proceeds for 4 h. Under the same reaction time, the removal efficiency of TOC is only 23.7% and 1.0% for Fe$_1$/C-CN photocatalysis and Fe$_1$/C-CN Fenton-like systems, respectively. The result strongly suggests that the Fe$_1$/C-CN photo-Fenton-like catalyst can not only degrade but also mineralize the recalcitrant organic micropollutants efficiently, and its mineralization ability greatly surpasses its single photocatalysis or heterogeneous Fenton-like system. The excellent mineralization ability of the Fe$_1$/C-CN photo-Fenton-like catalyst is further proved by monitoring the concentration changes of acetic acid (AA), formic acid (FA) and NO$_3^-$ anion. AA and FA are the important intermediates generated in PNP/Fe$_1$/C-CN photocatalysis or photo-Fenton-like degradation processes. Herein, AA and FA are identified by ion chromatography (IC, Fig. S10), and then their concentrations are determined quantitatively. In order to determine the concentration of AA and FA accurately by IC, a higher initial concentration (20 mg L^{-1}) of PNP is applied. As can be seen in Fig. 4h and Fig. S10, in PNP/Fe$_1$/C-CN photo-Fenton-like system, at the beginning of the reaction, the concentrations of AA and FA increase instantly, indicating continuous cleavage of aromatic rings of PNP. After the reaction carries out for 1 and 6 h, the concentration of FA and AA reaches the maximum, i.e., 3.9 and 14.1 mg L^{-1}, respectively. Further prolonging the reaction time, the concentrations of FA and AA begin to

decrease, suggesting that FA and AA are continuously mineralized to CO$_2$ and H$_2$O. In the Fe$_1$/C-CN photocatalysis system, the yielded AA (0.3 mg L^{-1}) and FA (0.6 mg L^{-1}) are obviously less even after the reaction performs for 8 h. NO$_3^-$ anion is another final product of PNP degradation, in PNP/Fe$_1$/C-CN photo-Fenton-like system, the concentration of NO$_3^-$ anion increases rapidly as prolonging the reaction time, and over period of 4 h, the concentration of NO$_3^-$ anion reaches up to 4.5 mg L^{-1} (Fig. 4i), which accounts for 100% cleavage of C−N bond in PNP molecule. However, under the same reaction time, only 40% cleavage of C−N bond (NO$_3^-$ anion concentration of 1.8 mg L^{-1}) is achieved in PNP/Fe$_1$/C-CN photocatalysis system.

Single Fe atom photo-Fenton-like catalysts with robust durability in the long-term remediation of organic micropollutants are vital for implementing practical applications. Owing to their high surface energy, during the treatment of organic micropollutants in wastewater, single Fe atoms in photo-Fenton-like catalysts always tend to move and aggregate into clusters or even nanoparticles; additionally, Fe leaching to reaction system is generally inevitable during repetitive catalytic cycles. Both factors lead to the notably decreased reusability of single Fe atom photo-Fenton-like catalysts [39]. Therefore, the reusability is another important performance of Fe$_1$/C-CN photo-Fenton-like catalyst. To evaluate the reusability, Fe$_1$/C-CN photo-Fenton-like catalytic oxidation of PNP reaction is recycled for five times. As displayed in Fig. 5a, after five times' catalytic cycles, the activity loss is negligible, and over period of 90 min, the removal efficiency of PNP is 99.3 (1st), 99.2 (2nd), 98.0 (3rd), 99.4 (4th) and 98.1% (5th), respectively. The result confirms the robust reusability of Fe$_1$/C-CN photo-Fenton-like catalyst in the long-term remediation of organic micropollutants. To account for this unique catalytic reusability, a series of characterization methods are applied for the five time spent Fe$_1$/C-CN photo-Fenton-like catalyst. The structural characterizations including XRD (Fig. 5b), FT-IR (Fig. 5c) and Fe 2p XPS (Fig. 5d) indicate that the spent Fe$_1$/C-CN photo-Fenton-like catalyst can maintain well its phase and chemical structure integrity; meanwhile, the coexistence of ≡Fe(II) and ≡Fe(III) species is ascertained with the peak intensity ratio of ≡Fe(II)/≡Fe(III) of 0.53, similar to that of the fresh Fe$_1$/C-CN (0.59). HAADF-STEM observation reveals that uniformly dispersed single Fe atoms still exist on the spent Fe$_1$/C-CN catalyst, and the agglomeration of Fe SAs after five times' catalytic cycles is hardly observed (Fig. 5e and f). Finally, the leaching of Fe to the reaction medium is analyzed by an ICP-MS, and the determined Fe content is below the detected limit (1.0 ng mL^{-1}) even after five catalytic cycles. The unique catalytic reusability of Fe$_1$/C-CN originates from the strong interlayer Fe−N coordination interactions, which firmly stabilize Fe SAs on C-CN support to not only avoid the agglomeration but also inhibit the leakage.

Next, from the perspective of industrial applications of Fe$_1$/C-CN in removal of recalcitrant organic micropollutants in wastewater, the experimental parameters, such as pH value, DOM and H$_2$O$_2$ dosage, are explored individually. Additionally, the treatment of pharmaceutical wastewater is also taken into account. As shown in Fig. 6a, 100% of PNP removal efficiency is achieved in Fe$_1$/C-CN photo-Fenton-like system after the reaction proceeds for 15, 60 and 90 min, respectively, at pH = 2.9, 5.6 and 7.5. However, further increasing pH to 9.9, only 79.0% of PNP is degraded after the reaction proceeds for 90 min. The result suggests that Fe$_1$/C-CN exhibits enhanced photo-Fenton-like performance under acidic condition, which is probably attributed to the increased redox potential of •OH radicals at lower pH values (e.g., 2.80 V at pH 3.0 and 1.90 V at pH 7.0) [40]. Nevertheless, Fe$_1$/C-CN still shows a wide pH window (2.9−7.5) for the efficient removal of PNP under visible-light irradiation.

DOM consists of abundant functional groups, such as carboxyl, phenolic, quinones and aromatics. These groups show unpredictable effects on the catalytic oxidation performance of photo-Fenton-like catalysts [41]. Here, Suwannee River Fulvic Acid (SRFA) and Suwannee River Humic Acid (SRHA) are chosen as the representative DOM to study their influence on the oxidation performance of Fe$_1$/C-CN
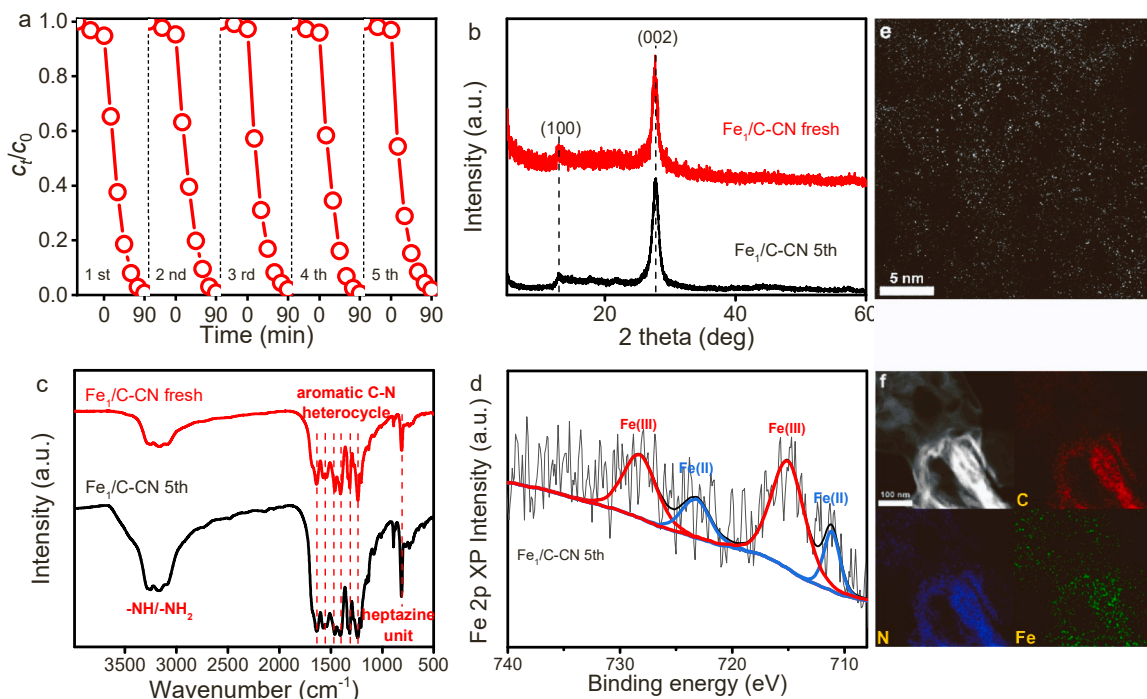
Fig. 5. (a) Reusability of the Fe$_1$/C-CN in photo-Fenton-like degradation of PNP. Catalyst amount 50 mg; $c_0 = 10$ mg L^{-1}; volume 50 mL; $c_{(H2O2)} = 50$ mmol L^{-1}; $\lambda > 400$ nm. (b) XRD, (c) FT-IR spectra, (d) Fe 2p XPS spectrum, (e) HAADF-STEM images and (f) element mapping of five time spent Fe$_1$/C-CN.
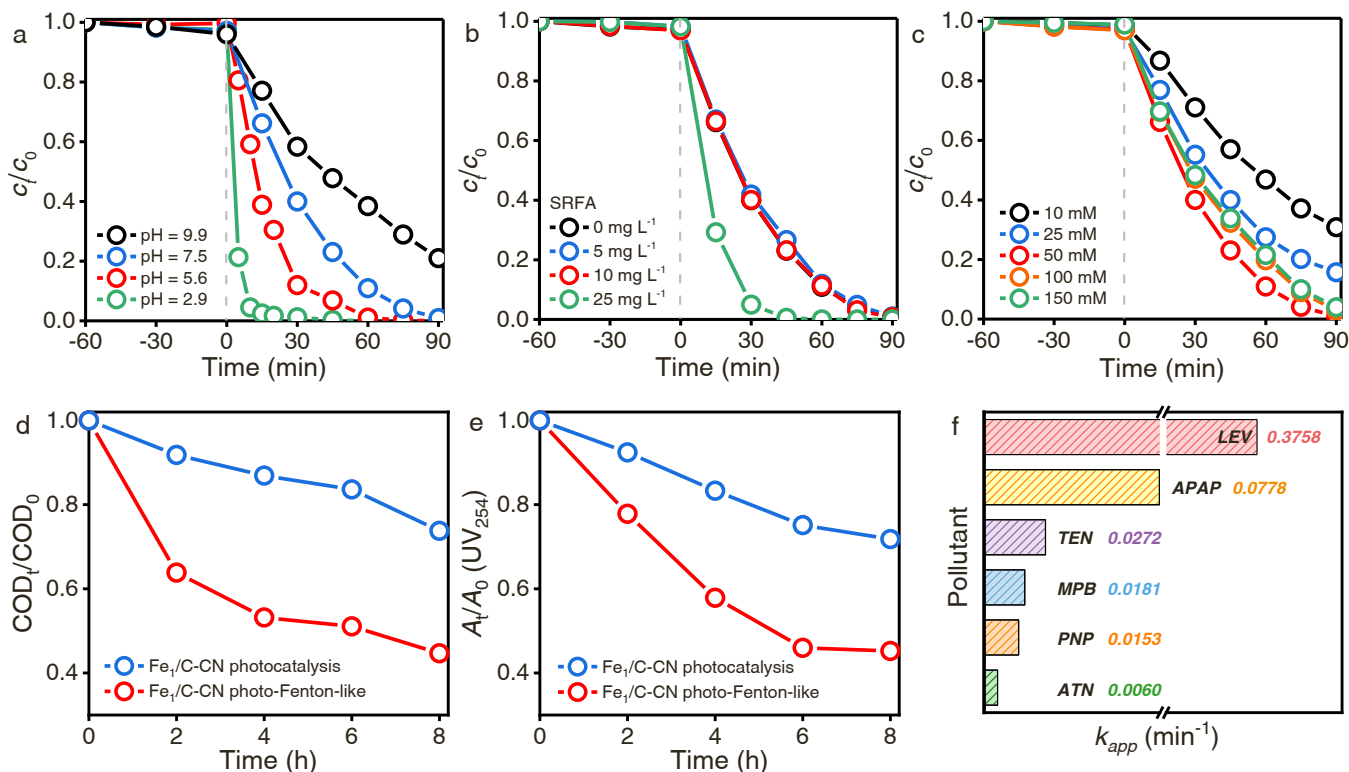

Fig. 6. Influence of (a) initial pH, (b) DOM and (c) H$_2$O$_2$ dosages on the photo-Fenton-like degradation efficiency of Fe$_1$/C-CN towards PNP. Catalyst amount 50 mg; $c_0 = 10$ mg L^{-1}; volume 50 mL; $\lambda > 400$ nm. Changes of (d) COD and (e) A (UV$_{254}$) during the process of photo-Fenton-like treatment of pharmaceutical wastewater over Fe$_1$/C-CN. Catalyst amount 50 mg; volume 50 mL; initial COD $= 70.7$ mg L^{-1}; A_0 (UV$_{254}$) $= 0.6563$; $c_{(H2O2)} = 50$ mmol L^{-1}; $\lambda > 320$ nm. (f) Pseudo-first-order kinetic constants of Fe$_1$/C-CN-catalyzed photo-Fenton-like reactions in the degradation of six mixed micropollutants. Catalyst amount 50 mg; $c_0 = 2$ mg L^{-1}; volume 50 mL; $c_{(H2O2)} = 50$ mmol L^{-1}; $\lambda > 320$ nm.

photo-Fenton-like catalyst in the degradation of PNP. As shown in Fig. 6b and Fig. S11, low concentrations (< 10 mg L^{-1}) of SRFA and SRHA have little impact on the removal efficiency of PNP. Further increasing the concentration of SRFA to 25 mg L^{-1}, the removal efficiency of PNP increases instead. The result is probably caused by the pH variation due to the presence of SRFA. At the low concentrations (5 and 10 mg L^{-1}) of SRFA and SRHA, the pH values of the reaction system are 6.9 and 6.3, respectively, close to the initial pH value of the reaction system (pH = 7.5). Correspondingly, the influence of SRFA at low concentrations on PNP removal efficiency is little. At a higher concentration (25 mg L^{-1}) of SRFA, the pH value of the reaction system changes to 5.8. The improved acidity in the reaction system can promote the oxidation ability of •OH radicals because of the increased redox potential of •OH radicals. Therefore, Fe$_1$/C-CN photo-Fenton-like system is recalcitrant to DOM.

Fig. 6c demonstrates the influence of H$_2$O$_2$ dosage on the photo-Fenton-like degradation efficiency of Fe$_1$/C-CN towards PNP. As increasing H$_2$O$_2$ dosage from 10 to 50 mmol L^{-1}, the removal efficiency of PNP significantly improves from 69.2% to 99.3%. The result reflects that the catalytic oxidation process of PNP in Fe$_1$/C-CN photo-Fenton-like system is mainly dominated by H$_2$O$_2$ activation. Further increasing H$_2$O$_2$ dosage to 100 and 150 mmol L^{-1}, the removal efficiency of PNP (97.2% and 96.0%) decreases slightly. This is due to the fact that higher H$_2$O$_2$ dosage may consume •OH radicals [42]. In order to obtain the maximal removal efficiency of PNP or MPB, H$_2$O$_2$ dosage is set at 50 mmol L^{-1} in current work.

Subsequently, Fe$_1$/C-CN photo-Fenton-like catalytic oxidation of organic micropollutants in pharmaceutical wastewater is tested by monitoring the changes of chemical oxygen demand (COD) and absorbance of aromatic and unsaturated organic compounds [A (UV$_{254}$)] in the reaction system, and the physicochemical parameters of pharmaceutical wastewater are summarized in Table S5. Changes of COD and A (UV$_{254}$) values during the process of photo-Fenton-like treatment of pharmaceutical wastewater over Fe$_1$/C-CN are monitored. As shown in Fig. 6d and e, with prolonging simulated sunlight irradiation time, a continuous decrease of COD value is observed, indicating gradual

elimination of organic micropollutants in pharmaceutical wastewater. After 8 h of light irradiation, the COD removal efficiency reaches up to 56.3%, twice higher than that of the Fe$_1$/C-CN photocatalysis system; simultaneously, the change trend of A (UV$_{254}$) values is consistent with that of COD, and over period of 8 h light irradiation, the A (UV$_{254}$) values decrease by 56.8% and 28.2% in Fe$_1$/C-CN photo-Fenton-like and photocatalysis systems, respectively. Therefore, Fe$_1$/C-CN catalyst also exhibits a remarkably high photo-Fenton-like degradation and mineralization efficiency towards organic micropollutants in pharmaceutical wastewater, outperforming its photocatalytic activity. To further evaluate the excellent catalytic oxidation performance of Fe$_1$/C-CN photo-Fenton-like system in the remediation of recalcitrant organic micropollutants in pharmaceutical wastewater, a mixture of six emerging organic micropollutants like LEV, TEN, MPB, PNP, ATN and APAP is added to pharmaceutical wastewater. As shown in Fig. S12, Fe$_1$/C-CN still exhibits the notably high photo-Fenton-like catalytic oxidation activity towards the degradation of mixed micropollutants in wastewater, and the removal efficiency of LEV, APAP, TEN, MPB, PNP and ATN reaches up to 100.0%, 100.0%, 100.0%, 100.0%, 100.0% and 71.0% after the reaction proceeds for 10, 50, 120, 180, 180 and 180 min, respectively, and the determined corresponding k_{app} value is 0.3758, 0.0778, 0.0272, 0.0181, 0.0153 and 0.0060 min^{-1}, respectively (Fig. 6f).

3.3. Insight into the photo-Fenton-like reaction mechanism

To gain an in-depth insight into the catalytic reaction mechanism of Fe$_1$/C-CN photo-Fenton-like system and to reveal the structure-performance relationship at the atomic scale, various characterization techniques and theoretical calculations are applied. At first, the ROSs generated in C-CN, Fe$_1$/C-CN and Fe$_1$/C-CN + H$_2$O$_2$ (50 mmol L^{-1}) systems are directly identified by an *in-situ* DMPO- and TEMP-trapping ESR spectroscopy method under Xe lamp irradiation. As shown in Fig. 7a−c, in C-CN system, the characteristic signals of DMPO−•O$_2^-$ and TEMP−^{1}O$_2$ adducts are observed, but the DMPO−•OH adduct signal is absent. Comparably, in Fe$_1$/C-CN system, the characteristic signals of
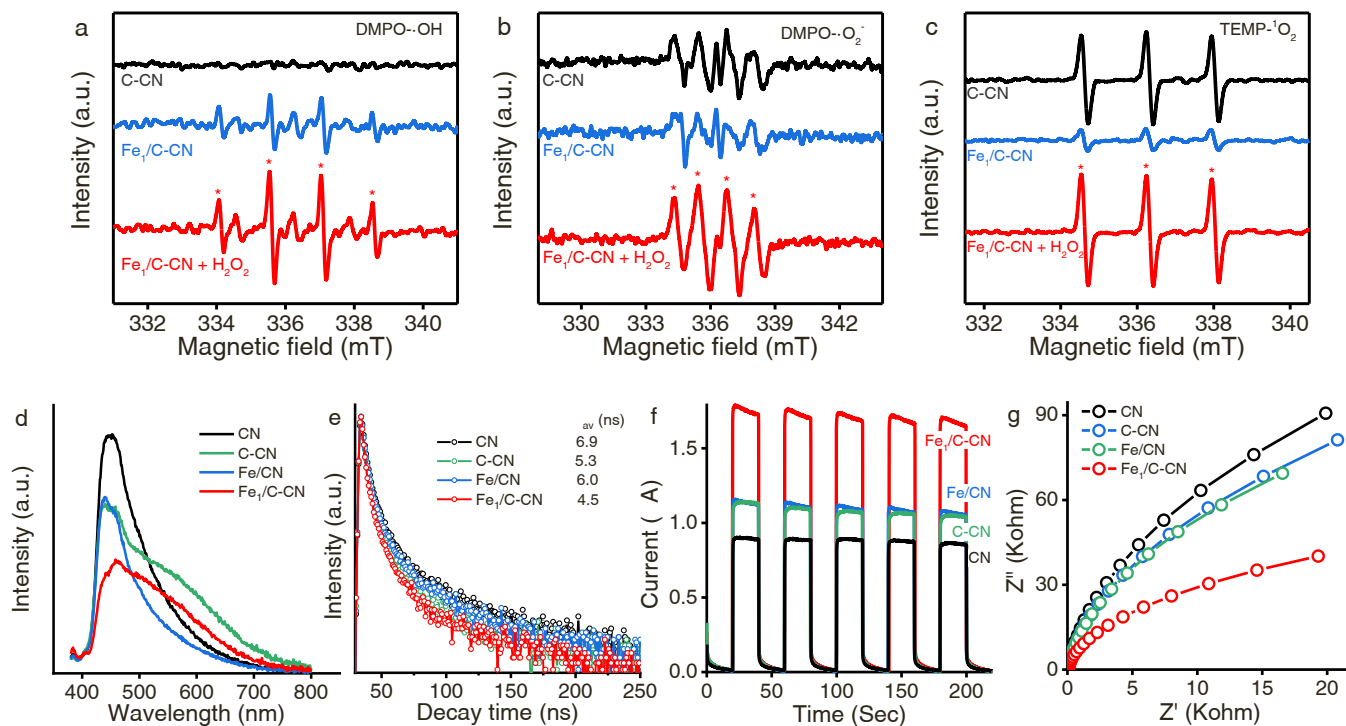
Fig. 7. DMPO- and TEMP-trapping ESR spectra of C-CN and Fe$_1$/C-CN for (a) DMPO-•OH adduct, (b) DMPO-•O$_2^-$ adduct and (c) TEMP-^{1}O$_2$ adduct under Xe lamp irradiation. (d) Steady-state PL emission and (e) TRPD spectra, (f) transient photocurrent responses and (g) EIS Nyquist plots of various g-C$_3$N$_4$-based materials.

DMPO−•OH, DMPO−•O$_2^-$ and TEMP−^{1}O$_2$ adducts are all found, indicating the formation of •OH, •O$_2^-$ and ^{1}O$_2$ species after the introduction of interlayer single-atomic Fe−N$_4$ sites on C-CN. In Fe$_1$/C-CN + H$_2$O$_2$ (50 mmol L^{-1}) system, remarkably increased amount of •OH, •O$_2^-$ and ^{1}O$_2$ species are produced, evidenced by the obviously enhanced signals of DMPO−•OH, DMPO−•O$_2^-$ and TEMP−^{1}O$_2$ adducts.

Afterwards, the separation and transfer kinetics of the photoexcited charges over CN, C-CN, Fe/CN and Fe$_1$/C-CN are investigated by photoluminescence (PL) spectroscopy analysis. In the steady-state PL spectra (Fig. 7d), CN exhibits a strong PL emission peak at 447 nm, reflecting the high radiative recombination probability of charges [43]. Compared with CN, the emission peak intensity of C-CN significantly decreases, indicating that the introduction of graphitic C$_{ring}$ can suppress the radiative recombination of charges by facilitating electron transfer. The PL emission peak of Fe/CN or Fe$_1$/C-CN is reduced obviously as compared with CN or C-CN, suggesting that the introduction of Fe sites can further inhibit the recombination of charges due to electron transfer from N atoms to Fe atoms. Particularly, owing to the formation of strong interlayer Fe−N coordination bonds, the Fe$_1$/C-CN exhibits more obvious decrease in PL emission intensity with respect to its C-CN support. Time-resolved fluorescence decay (TRPD) spectra are further measured to probe the charge separation and transport dynamics of the above catalysts, and the result is presented in Fig. 7e and Table S6. The average PL lifetime decay (τ_{av}) of CN, C-CN, Fe/CN and Fe$_1$/C-CN is 6.9, 5.3, 6.0 and 4.5 ns, respectively. The shortest PL lifetime decay of Fe$_1$/C-CN implies it has the fastest charge separation and transport dynamics among four catalysts.

Surface and bulk charge carrier separation and transfer efficiency is evaluated by photoelectrochemical tests. As shown in Fig. 7f, four tested samples all produce prompt and reproducible transient photocurrent responses, in which the Fe$_1$/C-CN produces the highest photocurrent response. Electrochemical impedance spectroscopy (EIS) testing aligns with the above result, and Fe$_1$/C-CN with the smallest curvature diameter of the Nyquist cycle exhibits the smallest charge transfer resistance (Fig. 7g). Both results confirm that the Fe$_1$/C-CN shows the highest charge carrier separation and transfer efficiency among the tested catalysts.

Contribution of interlayer single-atomic Fe−N$_4$ sites to the accelerated charge carrier separation and transport dynamics of Fe$_1$/C-CN is further clarified forcefully by comparison of *in-situ* femtosecond time-resolved transient absorption (fs-TA) spectroscopy analysis results of C-CN and Fe$_1$/C-CN (Fig. 8). Time-dependent 3D contour plots of fs-TA spectra shown in Fig. 8a and b indicate that C-CN and Fe$_1$/C-CN exhibit a narrow and negative profile from 450 to 490 nm, attributing to the stimulated emission (SE); meanwhile, they also possess a broad and positive signal in the region of 490−700 nm, which corresponds to the excited-state absorption (ESA) process of the photogenerated electrons, holes, or electron-hole pairs. Generally, SE reflects the recombination of electrons and holes, while a stronger ESA signal indicates the faster charge carrier separation and transport dynamics [44]. In comparison of C-CN, Fe$_1$/C-CN exhibits an enhanced ESA signal. To study the spectral evolution kinetics, the absorption decay of C-CN and Fe$_1$/C-CN from fs-TA spectra at different probe delays (from 1.4 ps to 1 ns) is provided (Fig. 8c and d), which shows continuous absorption decay with the time for both samples; furthermore, Fe$_1$/C-CN shows broader and notably enhanced ESA signal intensities than those of C-CN, highlighting the improved charge carrier separation and transport dynamics due to the introduction of interlayer single-atomic Fe−N$_4$ sites. To study the kinetics decay processes of ESA, the fs-TA kinetic decay traces of C-CN and Fe$_1$/C-CN are fitted at the selective wavelengths, 640 and 681 nm (Fig. 8e and f), and the time fitting parameters (τ_1, τ_2 and τ_3) are summarized in Table S7. The parameters of τ_1, τ_2 and τ_3 are related to charge carrier recombination, shallow and deep charge carrier trapping process, respectively [45]. Deep charge carrier trapping is a long process with large τ_3 value, and thereby charge carrier recombination and shallow charge carrier trapping are the main concerned parameters to evaluate the kinetics decay process of ESA. In comparison of C-CN with the time parameters of 0.04 (τ_1) and 1.47 ps (τ_2) at 640 nm as well as 0.03 (τ_1) and 2.11 ps (τ_2) at 681 nm, longer time parameters of Fe$_1$/C-CN are obtained, and they are 0.08 (τ_1) and 2.53 ps (τ_2) at 640 nm as well as 0.16 (τ_1) and 2.51 ps (τ_2) at 681 nm. More long-lived charge carrier recombination (τ_1) and shallow charge trapping (τ_2) of Fe$_1$/C-CN than C-CN confirm effective ESA survival, corresponding to more abundant free electrons and holes existing in Fe$_1$/C-CN system.

All of the above tests indicate that the introduction of graphitic C$_{ring}$ and the formation of strong interlayer single-atomic Fe−N$_4$ coordination
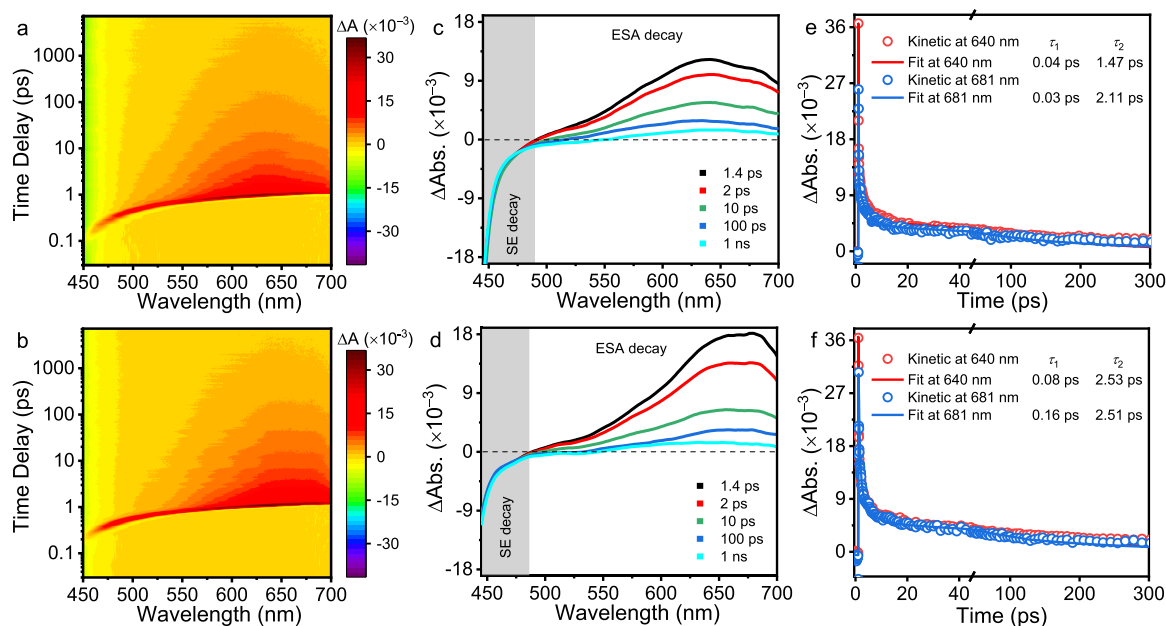

Fig. 8. Photogenerated charge carrier dynamics analysis by fs-TA spectroscopy. Time-dependent 3D contour plots of fs-TA spectra for (a) C-CN and (b) Fe$_1$/C-CN in the initial time window of 8 ns under 385 nm fs laser pulses. The representative absorption decay (Abs.) from fs-TA spectra at different probe delays for (c) C-CN and (d) Fe$_1$/C-CN. Kinetics decay process from fs-TA spectra observed at 640 and 681 nm for (e) C-CN and (f) Fe$_1$/C-CN and their corresponding tri-exponential decay fitted curves.

sites in Fe$_1$/C-CN catalyst significantly boosts the separation and transfer kinetics of the photogenerated charges, which is further proved by the calculated charge density difference (CDD) distribution of Fe$_1$/C-CN based on the proposed optimized structural model illustrated in Fig. 2m. CDD offers electronic density redistributions on the catalyst after being photoexcited from ground state to the first excited state. As illustrated in Fig. 9a and b, from the top and side views of CDD distribution it is clearly observed that Fe$_1$/C-CN shows an optimized distribution of the photogenerated electrons after light irradiation. Namely, electrons accumulate around Fe SAs and interlayer Fe−N coordination bonds (yellow regions), while the electronic density around C and N atoms becomes significantly lower. The result highlights a complete electron transfer from sp^2-hybridized N atoms of C-CN to empty d orbital of Fe atoms. This interlayer electron transfer through single-atomic Fe−N$_4$ sites greatly promotes charge separation, which is capable of providing plentiful free electrons to significantly accelerate the regeneration of ≡Fe(II) and thus interfacial efficient H$_2$O$_2$ activation; meanwhile, the formation of •OH, •O$_2^-$ and ^{1}O$_2$ via Fe$_1$/C-CN photocatalysis is also facilitated due to the presence of abundant free electrons and holes in the system.

Combination of the above characterization results and theoretical simulations, the heterogeneous photo-Fenton-like reaction mechanism of Fe$_1$/C-CN in the oxidation of organic micropollutants is put forward. Fe$_1$/C-CN-based heterogeneous photo-Fenton-like system has a dual role of photocatalysis and interfacial heterogeneous Fenton-like catalysis, and abundant photoexcited electrons and holes significantly facilitate the photocatalysis and interfacial heterogeneous Fenton-like catalysis processes simultaneously. As illustrated in Fig. 9c, before visible-light irradiation, H$_2$O$_2$ molecule with a smaller diameter of 0.25−0.28 nm [46] can readily diffuse into the interlayer of C-CN (interlayer distance of C-CN is 0.32 nm) and/or cross the "six-fold cavity" (the calculated diameter of the incircle in the "six-fold cavity" of C-CN is 0.48 nm,

Fig. S13), and thus it can reach the Fe sites confined in the interlayer of Fe$_1$/C-CN for subsequent activation process. Under visible-light irradiation, Fe$_1$/C-CN with E_g value of 2.65 eV is excited to generate photoexcited charges (h$^+$−e$^-$ pairs, Eq. 3). Next, the separation and transfer of the charges occurs, and the sluggish charge carrier separation and transfer dynamics on g-C$_3$N$_4$ is greatly boosted by the strong interlayer single-atomic Fe−N$_4$ coordination sites and C$_{ring}$-induced internal electric field. Accordingly, a novel and atomic-scale interlayer electron transfer channel in Fe$_1$/C-CN is established to direct the migration of electrons from sp^2-hybridized N atoms to empty d orbit of Fe atoms efficiently, which finally yields long-lived free photogenerated electrons and holes. Meanwhile, ≡Fe(III) in Fe$_1$/C-CN is reduced to ≡Fe(II) (Eq. 4). Thus, insufficient redox cycle of ≡Fe(III) ↔ ≡Fe(II) is stimulated by the injection of photoexcited electrons to ensure efficient H$_2$O$_2$ activation, which is the prerequisite to facilitate the generation of plentiful •OH radicals (Eqs. 5 and 6). In a parallel process, •O$_2^-$ anion radicals are yielded by the reduction of dioxygen molecules with the photogenerated electrons in Fe$_1$/C-CN photocatalysis system (Eq. 7); additionally, although •OH radicals are hardly generated in Fe$_1$/C-CN photocatalysis system via a direct hole oxidation of OH$^-$/H$_2$O because the VB edge potential of Fe$_1$/C-CN (+2.14 V $vs.$ NHE) is less positive than the redox potential of OH$^-$/•OH (+2.40 V $vs.$ NHE) or H$_2$O/•OH (+2.72 V $vs.$ NHE) [47], •OH radicals can be indirectly produced in this system by a two electron reduction of •O$_2^-$ anion radicals owing to the presence of long-lived free electrons (Eq. 8). The generation of ^{1}O$_2$ is due to the combination of •O$_2^-$ anion radicals with h$^+$ (Eq. 9). Since the presence of plentiful long-lived free electrons, •O$_2^-$ anion radicals can further be reduced by the free electrons to •OH radicals in Fe$_1$/C-CN photocatalysis system, correspondingly, the number of the formed ^{1}O$_2$ decreases as compared with C-CN system (Fig. 7c). Under the attack of •OH radicals, •O$_2^-$ anion radicals and ^{1}O$_2$, the target organic micropollutants are deeply oxidized to CO$_2$, H$_2$O and inorganic anion (Eq. 10).
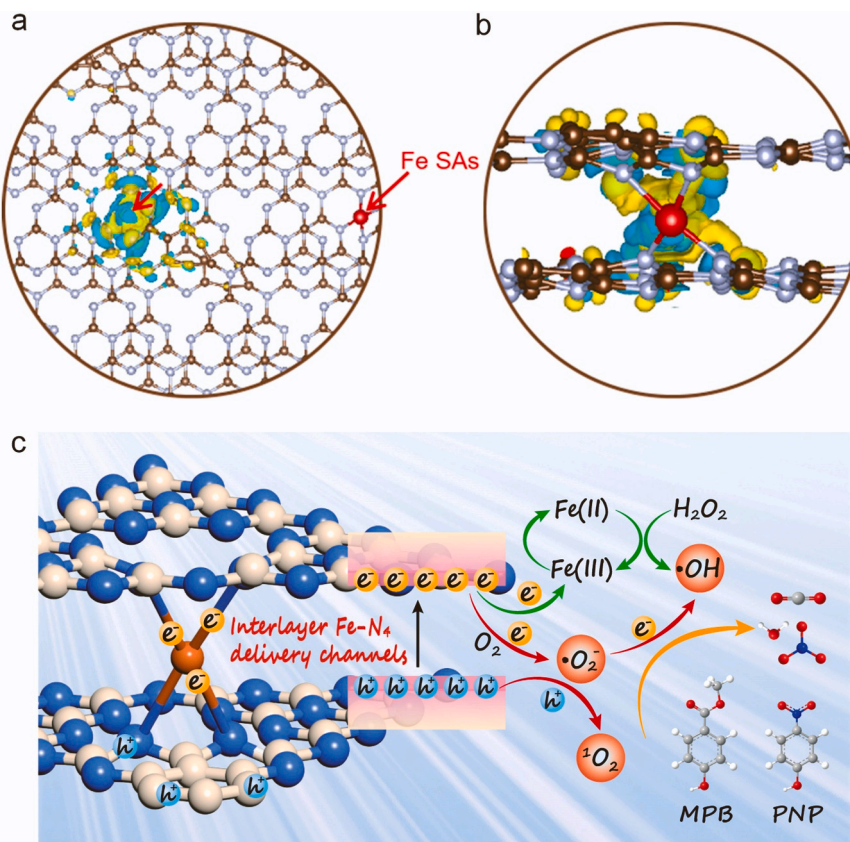

Fig. 9. Charge density difference analysis of Fe$_1$/C-CN (a: top view; b: side view). Cyan and yellow regions indicate electron depletion and accumulation, respectively. (c) Schematic illustration of the mechanism of photo-Fenton-like degradation of organic micropollutants over Fe$_1$/C-CN.

$$Fe_1/C\text{-}CN \xrightarrow{\text{visible-light}} Fe_1/C\text{-}CN\ (e^- + h^+) \tag{3}$$

$$\equiv Fe(III) + e^- \longrightarrow \equiv Fe(II) \tag{4}$$

$$\equiv Fe(II) + H_2O_2 \longrightarrow \equiv Fe(III) + \bullet OH + OH^- \tag{5}$$

$$\equiv Fe(III) + H_2O_2 \longrightarrow \equiv Fe(II) + HO_2\bullet + H^+ \tag{6}$$

$$e^- + O_2 \longrightarrow \bullet O_2^- \tag{7}$$

$$\bullet O_2^- + 2e^- + 2H^+ \longrightarrow \bullet OH + OH^- \tag{8}$$

$$\bullet O_2^- + h^+ \longrightarrow {}^1O_2 \tag{9}$$
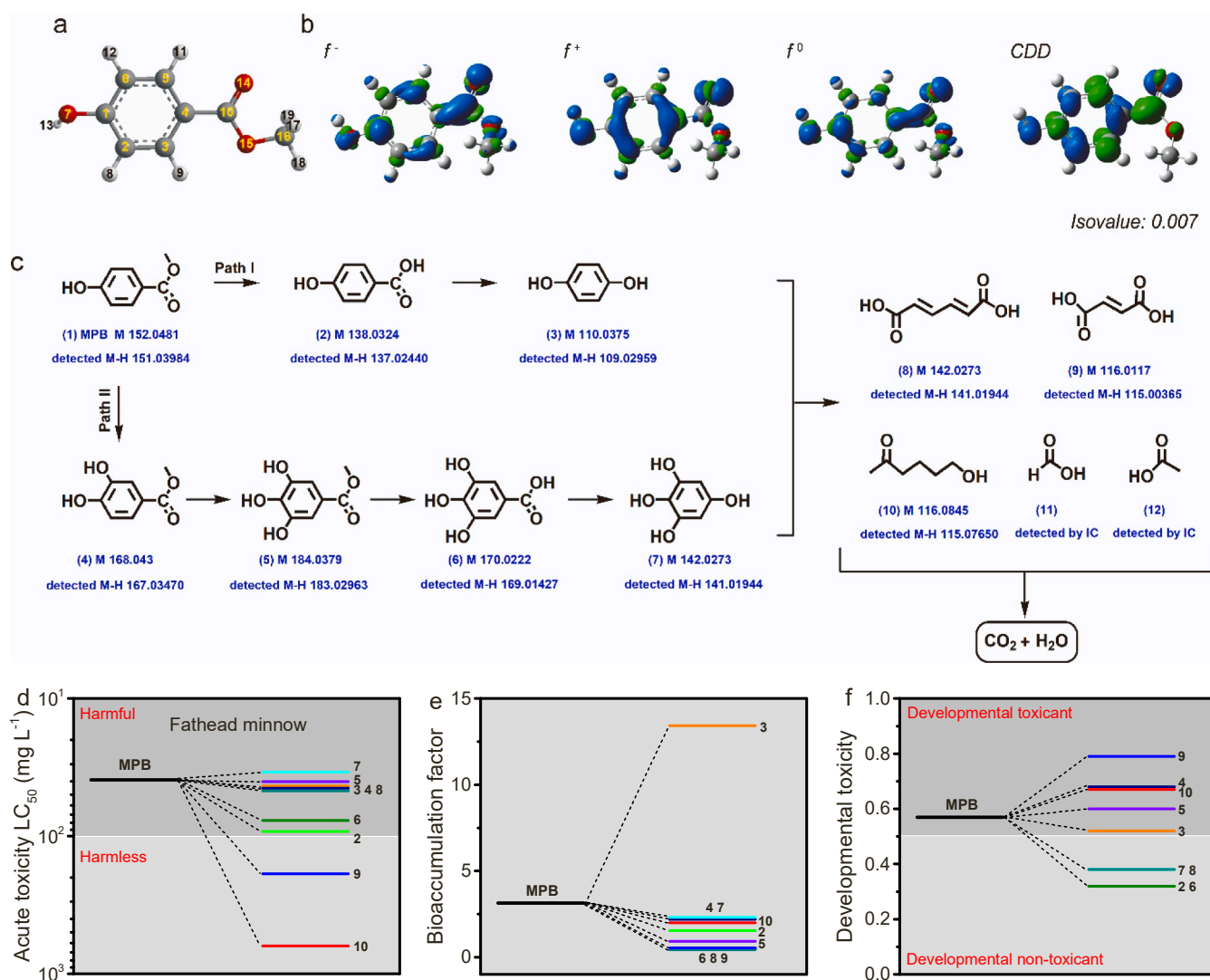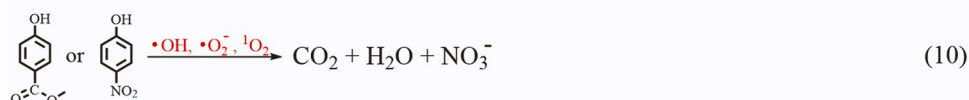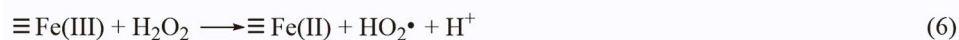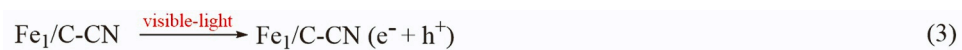

$$(10)$$

Fig. 10. (a) The optimized molecule structure and (b) the isosurface of Fukui indices of MPB. (c) The proposed pathway of visible-light photo-Fenton-like degradation of MPB over Fe$_1$/C-CN. (d) Acute toxicity, (e) bioaccumulation factor and (f) developmental toxicity of MPB and the identified degradation intermediates.

The other important factor determined the outstanding heterogeneous photo-Fenton-like catalytic oxidation activity of Fe_1/C-CN is the maximum Fe atoms utilization efficiency for the reaction, originating from highly dispersed interlayer single-atomic $Fe-N_4$ coordination sites on C-CN with specific coordinatively unsaturated sites. Therefore, the synergistic effect of greatly boosted photoexcited charge separation and transfer dynamics and the maximum Fe atoms utilization efficiency significantly accelerates the regeneration of ≡Fe(II) and thus interfacial efficient H_2O_2 activation of Fe_1/C-CN, leading to Fe_1/C-CN photo-Fenton-like catalyst eminent degradation and mineralization capacity to recalcitrant organic micropollutants. Although Fe/CN photo-Fenton-like system can also generate a certain amount of ROS such as •OH, •O_2^- and $^1O_2$, the absence of the above two unique advantages renders it obviously lower photo-Fenton-like catalytic oxidation activity in the degradation of organic micropollutants.

3.4. Possible degradation pathway and toxicity estimation

To achieve deep insights into the degradation process of MPB and PNP in the Fe_1/C-CN photo-Fenton-like system, the degradation pathways of MPB and PNP are studied by Fukui function analysis (Figs. 10 and 11) as well as IC and LC-MS (Fig. S14) measurements. At first, the Fukui function of MPB is obtained to predict the possible reactive sites for attacking MPB, and the atoms with higher f^-, f^+ and f^0 values are more liable to be attacked by electrophilic species (h_{VB}^+ and $^1O_2$),

nucleophilic species (•O_2^- anion radicals) and radicals (•OH), respectively [48,49]; moreover, when the atoms possess both high f^- and f^+ values, condensed dual descriptor (CDD) is a comprehensive index of electrophilicity and nucleophilicity (Table S8 and Fig. 10a and b). Subsequently, combined with the above DFT calculations and the identified intermediates by IC (Fig. S10) and LC-MS (Fig. S14) generated during MPB degradation process over Fe_1/C-CN photo-Fenton-like catalyst, the possible degradation pathways for MPB are put forward (Fig. 10c). In path I, under continuous attack of ROSs, MPB molecule first suffers from demethylation to yield 4-hydroxybenzoic acid (Compound **2**). Then, C10 atom with both more positive CDD and f^0 values (0.0660 and 0.0698) is easily attacked by •O_2^- anion radicals and •OH radicals, leading to hydroquinone (Compound **3**). In path II, C2 and C6 atoms with more negative CDD values (−0.0288 and −0.0109) are highly vulnerable to being attacked by h_{VB}^+ and $^1O_2$ to produce methyl 3,4-dihydroxybenzoate (Compound **4**) and methyl 3,4,5-trihydroxybenzoate (Compound **5**). Compound **5** undergoes demethylation to yield 3,4,5-trihydroxybenzoic acid (Compound **6**). Subsequently, •O_2^- anion radicals and •OH radicals attack C10 atom to generate benzene-1,2,3,5-tetraol (Compound **7**). After successive oxidation, the aromatic rings are opened, leading to (2E,4E)-hexa-2,4-dienedioic acid (Compound **8**), fumaric acid (Compound **9**), 6-hydroxyhexan-2-one (Compound **10**), FA (Compound **11**) and AA (Compound **12**). Continuous prolonging visible-light irradiation time leads to the mineralization of the intermediates to CO_2 and H_2O.
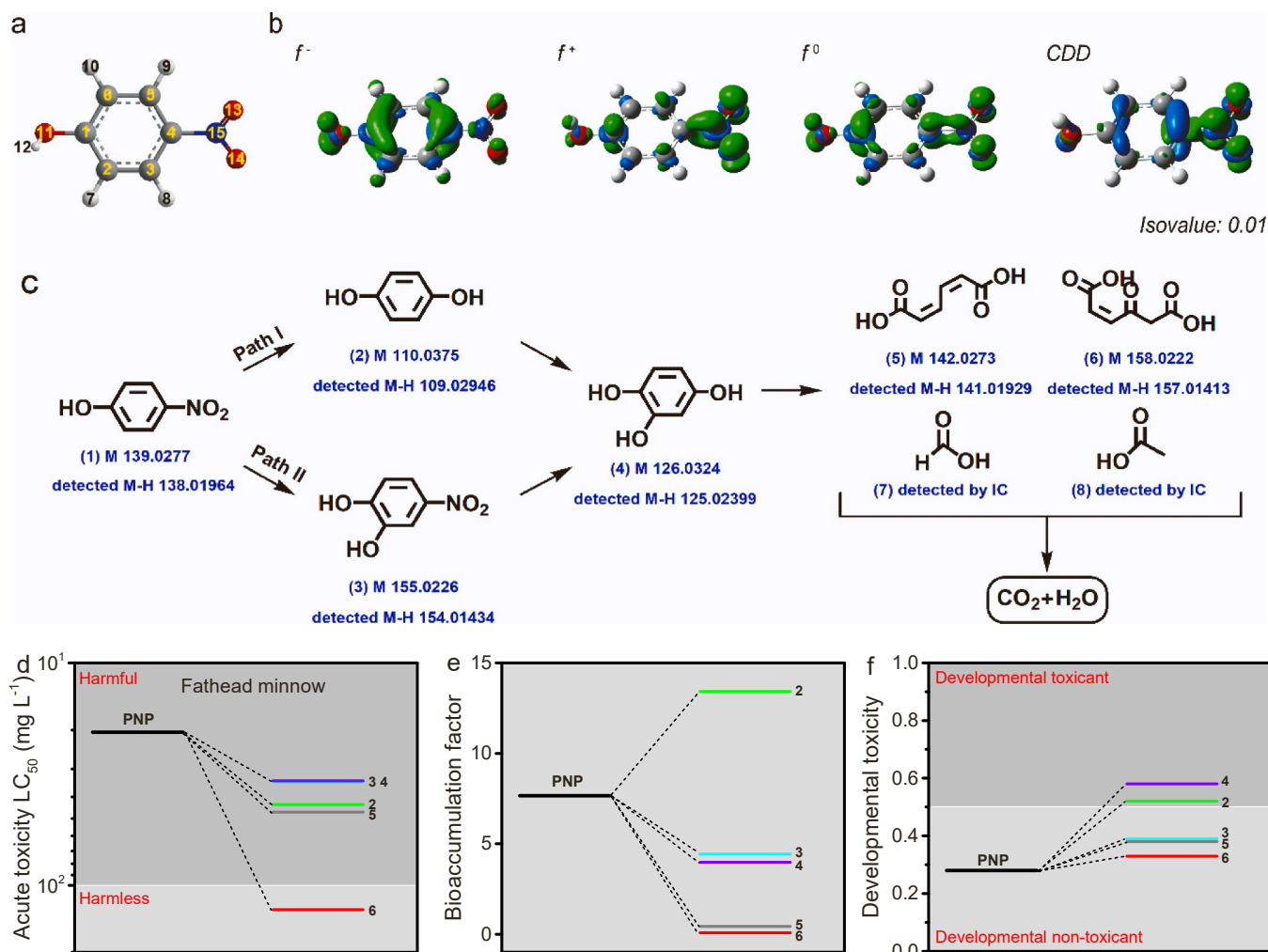

Fig. 11. (a) The optimized molecule structure and (b) the isosurface of Fukui indices of PNP. (c) The proposed pathway of visible-light photo-Fenton-like degradation of PNP over Fe_1/C-CN. (d) Acute toxicity, (e) bioaccumulation factor and (f) developmental toxicity of PNP and the identified degradation intermediates.

The acute toxicity, bioaccumulation factor and developmental toxicity of MPB and its degradation intermediates are then predicted through Toxicity Estimation Software Tool (T.E.S.T.) to evaluate the ecotoxicity risk during visible-light photocatalytic degradation of MPB in the Fe$_1$/C-CN photo-Fenton-like system (Fig. 10d–f, Table S9) [50, 51]. The lethal concentration of 50% (LC$_{50}$) of MPB for fathead minnow is 39.10 mg L^{-1}, which is considered as "Harmful". Nevertheless, most of the intermediates exhibit lower LC$_{50}$ values, especially for Compound **9** (187.87 mg L^{-1}) and Compound **10** (628.50 mg L^{-1}), and they are considered as "harmless" (Fig. 10d). The result reveals that the acute toxicity of MPB is significantly reduced after photo-Fenton-like degradation. Fig. 10e shows a lower bioaccumulation factor of most intermediates compared to MPB (3.13), reflecting the reduced bioaccumulation after photo-Fenton-like degradation. Furthermore, most degradation intermediates exhibit lower developmental toxicity compared to MPB, and they are categorized as developmental non-toxicants (Fig. 10f). These results indicate that further deep oxidation of MPB is necessary to eliminate toxic intermediates.

The pathways of visible-light degradation of PNP in the Fe$_1$/C-CN photo-Fenton-like system are also investigated by Fukui function, IC and LC-MS (Fig. 11a, b and Table S10, Figs. S10 and S14). In Fig. 11c, in path I, since C4 possesses more negative CDD and higher f^0 values (−0.0840 and 0.0816) as well as N15 with more positive CDD values (0.0896), they are highly attacked by the active species to yield hydroquinone (Compound **2**). Then, C2 atom with a more negative CDD value (−0.0322) is more easily attacked by h$_{VB}^+$ and $^1O_2$ to generate benzene-1,2,4-triol (Compound **4**). In path II, h$_{VB}^+$ and $^1O_2$ attack C2 atom to produce 4-nitrobenzene-1,2-diol (Compound **3**), further oxidation of Compound **3** yields Compound **4**. Then, aromatic ring of Compound **4** is opened, giving rise to (2Z,4Z)-hexa-2,4-dienedioic acid (Compound **5**), (Z)-4-oxohex-2-enedioic acid (Compound **6**), FA (Compound **7**) and AA (Compound **8**). Ultimately, the mineralization of PNP to CO$_2$, H$_2$O and NO$_3^-$ anion is achieved under further visible-light irradiation.

The ecotoxicity risk evaluation results are listed in Table S11. The LC$_{50}$ values of all PNP degradation intermediates are higher than PNP itself (Fig. 11d), indicating a significant reduction in acute toxicity for these intermediates. Fig. 11e reflects that the photo-Fenton-like degradation process effectively diminishes the bioaccumulation factor of most of the intermediates. The developmental toxicity of most of the intermediates decreases as the reaction proceeds and becomes a developmental non-toxicant (Fig. 11f). The above toxicity evaluation results further confirm the outstanding deep oxidation capacity of Fe$_1$/C-CN photo-Fenton-like catalyst, ensuring the effectively reduced ecotoxicity of recalcitrant organic micropollutants in wastewater after the degradation.

4. Conclusions

An *in-situ* approach of glucose-assistant supramolecule self-assembly of melamine and cyanuric acid in the presence of Fe(NO$_3$)$_3$ followed by thermal polymerization is developed to prepare carbon-rich g-C$_3$N$_4$ embedded interlayer single-atomic Fe−N$_4$ sites photo-Fenton-like catalyst (Fe$_1$/C-CN), in which glucose plays a pivotal role for chemically stabilizing single Fe atoms on carbon-rich g-C$_3$N$_4$ support by chelating Fe species and then forming strong interlayer Fe−N coordination bonding. The unique electronic structure of Fe$_1$/C-CN creates novel and atomic-scale interlayer electron transfer channels and graphitic C$_{ring}$ units-induced internal electric field. Thus, the sluggish charge carrier separation and transfer dynamics on g-C$_3$N$_4$ is greatly boosted, leading to abundant long-lived free photoexcited electrons and holes to not only significantly accelerate the regeneration of ≡Fe(II) and interfacial efficient H$_2$O$_2$ activation but also facilitate Fe$_1$/C-CN photocatalysis process. The synergistic effect of greatly accelerated photoexcited charge separation and transfer dynamics and the maximum Fe atom utilization efficiency results in the generation of ROSs including •OH radicals, •O$_2^-$ anion radicals and $^1O_2$ with obviously increased concentrations in Fe$_1$/

C-CN heterogeneous photo-Fenton-like catalytic system, which ensure it extraordinary degradation and mineralization capability towards recalcitrant organic micropollutants in both experimental water and pharmaceutical wastewater, effectively reducing their ecotoxicity. More importantly, Fe$_1$/C-CN also exhibits robust durability in the long-term remediation of organic micropollutants, originating from the strong interlayer Fe−N coordination bonding for stabilizing single Fe atoms on C-CN support to not only avoid their agglomeration but also inhibit their leakage.

CRediT authorship contribution statement

Lang Qin: Investigation, Data curation. **Jiaqi Meng:** Supervision. **Guang Yang:** Investigation. **Yue Pan:** Investigation. **Xinchun Gao:** Investigation. **Yuxin Yang:** Writing – original draft, Visualization. **Yihang Guo:** Conceptualization, Supervision, Writing – review & editing.

Declaration of Competing Interest

The authors declare that they have no known competing financial interests or personal relationships that could have appeared to influence the work reported in this paper.

Data Availability

Data will be made available on request.

Acknowledgements

Appendix A. Supporting information

Supplementary data associated with this article can be found in the online version at doi:10.1016/j.apcatb.2024.123695.

References

[1] T. Cui, L. Li, C. Ye, X. Li, C. Liu, S. Zhu, W. Chen, D. Wang, Heterogeneous single atom environmental catalysis: Fundamentals, applications, and opportunities, Adv. Funct. Mater. 32 (2022) 2108381, https://doi.org/10.1002/adfm.202108381.

[2] X. Wang, X. Zhang, Y. Zhang, Y. Wang, S.-P. Sun, W.D. Wu, Z. Wu, Nanostructured semiconductor supported iron catalysts for heterogeneous photo-Fenton oxidation: A review, J. Mater. Chem. A 8 (2020) 15513–15546, https://doi.org/10.1039/D0TA04541A.

[3] C. Liu, H. Dai, C. Tan, Q. Pan, F. Hu, X. Peng, Photo-Fenton degradation of tetracycline over Z-scheme Fe-g-C$_3$N$_4$/Bi$_2$WO$_6$ heterojunctions: Mechanism insight, degradation pathways and DFT calculation, Appl. Catal. B: Environ. 310 (2022) 121326, https://doi.org/10.1016/j.apcatb.2022.121326.

[4] J. Lin, W. Tian, Z. Guan, H. Zhang, X. Duan, H. Wang, H. Sun, Y. Fang, Y. Huang, S. Wang, Functional carbon nitride materials in photo-Fenton-like catalysis for environmental remediation, Adv. Funct. Mater. 32 (2022) 2201743, https://doi.org/10.1002/adfm.202201743.

[5] M. Liu, H. Xia, W. Yang, X. Liu, J. Xiang, X. Wang, L. Hu, F. Lu, Novel Cu-Fe bi-metal oxide quantum dots coupled g-C$_3$N$_4$ nanosheets with H$_2$O$_2$ adsorption-activation trade-off for efficient photo-Fenton catalysis, Appl. Catal. B: Environ. 301 (2022) 120765, https://doi.org/10.1016/j.apcatb.2021.120765.

[6] M. Qian, X.-L. Wu, M. Lu, L. Huang, W. Li, H. Lin, J. Chen, S. Wang, X. Duan, Modulation of charge trapping by island-like single-atom cobalt catalyst for enhanced photo-Fenton-like reaction, Adv. Funct. Mater. 33 (2023) 2208688, https://doi.org/10.1002/adfm.202208688.

[7] L. Su, P. Wang, X. Ma, J. Wang, S. Zhan, Regulating local electron density of iron single sites by introducing nitrogen vacancies for efficient photo-Fenton process, Angew. Chem. Int. Ed. 60 (2021) 21261–21266, https://doi.org/10.1002/anie.202108937.

[8] Y. Zhou, Y. Yu, Q. Zhang, X. Sun, J. Niu, Regulating electron distribution of Fe/Ni-N$_4$P$_2$ single sites for efficient photo-Fenton process, J. Hazard. Mater. 440 (2022) 129724, https://doi.org/10.1016/j.jhazmat.2022.129724.

[9] S. Dong, X. Chen, L. Su, Y. Wen, Y. Wang, Q. Yang, L. Yi, W. Xu, Q. Yang, P. He, Y. Zhu, Z. Lu, Integration of atomically dispersed Cu–N₄ sites with C₃N₄ for enhanced photo-Fenton degradation over a nonradical mechanism, ACS EST Eng. 3 (2023) 150–164, https://doi.org/10.1021/acsestengg.2c00261.

[10] F. Chen, X.-L. Wu, C. Shi, H. Lin, J. Chen, Y. Shi, S. Wang, X. Duan, Molecular engineering toward pyrrolic N-rich M-N₄ (M = Cr, Mn, Fe, Co, Cu) single-atom sites for enhanced heterogeneous Fenton-like reaction, Adv. Funct. Mater. 31 (2021) 2007877, https://doi.org/10.1002/adfm.202007877.

[11] S. Liu, D. Liu, Y. Sun, P. Xiao, H. Lin, J. Chen, X.-L. Wu, X. Duan, S. Wang, Enzyme-mimicking single-atom FeN₄ sites for enhanced photo-Fenton-like reactions, Appl. Catal. B: Environ. 310 (2022) 121327, https://doi.org/10.1016/j.apcatb.2022.121327.

[12] X.-L. Wu, S. Liu, Y. Li, M. Yan, H. Lin, J. Chen, S. Liu, S. Wang, X. Duan, Directional and ultrafast charge transfer in oxygen-vacancy-rich ZnO@single-atom cobalt core-shell junction for photo-Fenton-like reaction, Angew. Chem. Int. Ed. 62 (2023) e202305639, https://doi.org/10.1002/anie.202305639.

[13] Y. Yang, X. Li, C. Zhou, W. Xiong, G. Zeng, D. Huang, C. Zhang, W. Wang, B. Song, X. Tang, X. Li, H. Guo, Recent advances in application of graphitic carbon nitride-based catalysts for degrading organic contaminants in water through advanced oxidation processes beyond photocatalysis: a critical review, Water Res 184 (2020) 116200, https://doi.org/10.1016/j.watres.2020.116200.

[14] L. Cheng, H. Zhang, X. Li, J. Fan, Q. Xiang, Carbon-graphitic carbon nitride hybrids for heterogeneous photocatalysis, Small 17 (2021) 2005231, https://doi.org/10.1002/smll.202005231.

[15] M. Ren, X. Zhang, Y. Liu, G. Yang, L. Qin, J. Meng, Y. Guo, Y. Yang, Interlayer palladium-single-atom-coordinated cyano-group-rich graphitic carbon nitride for enhanced photocatalytic hydrogen production performance, ACS Catal. 12 (2022) 5077–5093, https://doi.org/10.1021/acscatal.2c00427.

[16] L. Zhao, Y. Zhang, L.-B. Huang, X.-Z. Liu, Q.-H. Zhang, C. He, Z.-Y. Wu, L.-J. Zhang, J. Wu, W. Yang, L. Gu, J.-S. Hu, L.-J. Wan, Cascade anchoring strategy for general mass production of high-loading single-atomic metal-nitrogen catalysts, Nat. Commun. 10 (2019) 1278, https://doi.org/10.1038/s41467-019-09290-y.

[17] J. Meng, X. Zhang, G. Yang, L. Qin, Y. Pan, Y. Guo, Porous cyclopentadiene unit-incorporated graphitic carbon nitride nanosheets for efficient photocatalytic oxidation of recalcitrant organic micropollutants in wastewater, J. Hazard. Mater. 460 (2023) 132365, https://doi.org/10.1016/j.jhazmat.2023.132365.

[18] D. Feng, Y. Cheng, J. He, L. Zheng, D. Shao, W. Wang, W. Wang, F. Lu, H. Dong, H. Liu, R. Zheng, H. Liu, Enhanced photocatalytic activities of g-C₃N₄ with large specific surface area via a facile one-step synthesis process, Carbon 125 (2017) 454–463, https://doi.org/10.1016/j.carbon.2017.09.084.

[19] J. Meng, X. Zhang, Y. Liu, M. Ren, Y. Guo, X. Yang, Y. Yang, Engineering of graphitic carbon nitride with simultaneous potassium doping sites and nitrogen defects for notably enhanced photocatalytic oxidation performance, Sci. Total Environ. 796 (2021) 148946, https://doi.org/10.1016/j.scitotenv.2021.148946.

[20] C. Su, M. Acik, K. Takai, J. Lu, S.J. Hao, Y. Zheng, P. Wu, Q. Bao, T. Enoki, Y. J. Chabal, K.P. Loh, Probing the catalytic activity of porous graphene oxide and the origin of this behaviour, Nat. Commun. 3 (2012) 1298, https://doi.org/10.1038/ncomms2315.

[21] W. Che, W. Cheng, T. Yao, F. Tang, W. Liu, H. Su, Y. Huang, Q. Liu, J. Liu, F. Hu, Z. Pan, Z. Sun, S. Wei, Fast photoelectron transfer in (C_ring)-C₃N₄ plane heterostructural nanosheets for overall water splitting, J. Am. Chem. Soc. 139 (2017) 3021–3026, https://doi.org/10.1021/jacs.6b11878.

[22] H. Kim, S. Gim, T.H. Jeon, H. Kim, W. Choi, Distorted carbon nitride structure with substituted benzene moieties for enhanced visible light photocatalytic activities, ACS Appl. Mater. Interfaces 9 (2017) 40360–40368, https://doi.org/10.1021/acsami.7b14191.

[23] Y. Liu, M. Ren, X. Zhang, G. Yang, L. Qin, Y. Pan, J. Meng, Y. Guo, Ti–N coordination bonds boost Z-scheme interfacial charge transfer in TiO₂/C-deficient g-C₃N₄ heterojunctions for enhanced photocatalytic phenolic pollutant degradation, Appl. Surf. Sci. 614 (2023) 156118, https://doi.org/10.1016/j.apsusc.2022.156118.

[24] Y. Huang, D. Li, Z. Fang, R. Chen, B. Luo, W. Shi, Controlling carbon self-doping site of g-C₃N₄ for highly enhanced visible-light-driven hydrogen evolution, Appl. Catal. B: Environ. 254 (2019) 128–134, https://doi.org/10.1016/j.apcatb.2019.04.082.

[25] X. Wang, L. Sang, L. Zhang, G. Yang, Y. Guo, Y. Yang, Controllable synthesis for carbon self-doping and structural defect co-modified g-C₃N₄: Enhanced photocatalytic oxidation performance and the mechanism insight, J. Alloy. Compd. 941 (2023) 168921, https://doi.org/10.1016/j.jallcom.2023.168921.

[26] G. Lei, Y. Tong, L. Shen, F. Liu, Y. Xiao, W. Lin, Y. Zhang, C. Au, L. Jiang, Highly active and sulfur-resistant Fe–N₄ sites in porous carbon nitride for the oxidation of H₂S into elemental sulfur, Small 16 (2020) 2003904, https://doi.org/10.1002/smll.202003904.

[27] X. Zhang, G. Yang, J. Meng, L. Qin, M. Ren, Y. Pan, Y. Yang, Y. Guo, Acetamide- or formamide-assisted in situ approach to carbon-rich or nitrogen-deficient graphitic carbon nitride for notably enhanced visible-light photocatalytic redox performance, Small 19 (2023) 2208012, https://doi.org/10.1002/smll.202208012.

[28] X. Yang, L. Xu, X. Yu, W. Li, K. Li, M. Huo, Y. Guo, Enhanced photocatalytic activity of Eu₂O₃/Ta₂O₅ mixed oxides on degradation of rhodamine B and 4-nitrophenol, Colloids Surf. A: Physicochem. Eng. Asp. 320 (2008) 61–67, https://doi.org/10.1016/j.colsurfa.2008.01.019.

[29] J.C.M. Tempestti, H. Mohan, P. Muthukumar Sathya, S.-W. Lee, J. Venkatachalam, B.-T. Oh, K.-K. Seralathan, Detoxification of p-nitrophenol (PNP) using Enterococcus gallinarum JT-02 isolated from animal farm waste sludge, Environ. Res. 231 (2023) 116289, https://doi.org/10.1016/j.envres.2023.116289.

[30] J. Li, J. Jiang, S.Y. Pang, Y. Zhou, Y. Gao, Y. Yang, S. Sun, G. Liu, J. Ma, C. Jiang, L. Wang, Transformation of methylparaben by aqueous permanganate in the presence of iodide: kinetics, modeling, and formation of iodinated aromatic products, Water Res 135 (2018) 75–84, https://doi.org/10.1016/j.watres.2018.02.014.

[31] E. Ahmed, K. Nagaoka, M. Fayez, M.M. Abdel-Daim, H. Samir, G. Watanabe, Suppressive effects of long-term exposure to p-nitrophenol on gonadal development, hormonal profile with disruption of tissue integrity, and activation of caspase-3 in male Japanese quail (Coturnix japonica), Environ. Sci. Pollut. Res. 22 (2015) 10930–10942, https://doi.org/10.1007/s11356-015-4245-9.

[32] Y. He, W. Su, X. Zhai, L. Luo, T. Luan, L. Yang, Experimental and theoretical studies into the hydroxyl radical mediated transformation of propylparaben to methylparaben in the presence of dissolved organic matter surrogate, Water Res 204 (2021) 117623, https://doi.org/10.1016/j.watres.2021.117623.

[33] G. Li Puma, V. Puddu, H.K. Tsang, A. Gora, B. Toepfer, Photocatalytic oxidation of multicomponent mixtures of estrogens (estrone (E1), 17β-estradiol (E2), 17α-ethynylestradiol (EE2) and estriol (E3)) under UVA and UVC radiation: photon absorption, quantum yields and rate constants independent of photon absorption, Appl. Catal. B: Environ. 99 (2010) 388–397, https://doi.org/10.1016/j.apcatb.2010.05.015.

[34] I. Grčić, G. Li Puma, Photocatalytic degradation of water contaminants in multiple photoreactors and evaluation of reaction kinetic constants independent of photon absorption, irradiance, reactor geometry, and hydrodynamics, Environ. Sci. Technol. 47 (2013) 13702–13711, https://doi.org/10.1021/es403472e.

[35] F. Wang, J. Xu, Z. Wang, Y. Lou, C. Pan, Y. Zhu, Unprecedentedly efficient mineralization performance of photocatalysis-self-Fenton system towards organic pollutants over oxygen-doped porous g-C₃N₄ nanosheets, Appl. Catal. B: Environ. 312 (2022) 121438, https://doi.org/10.1016/j.apcatb.2022.121438.

[36] G. Li Puma, Modeling of thin-film slurry photocatalytic reactors affected by radiation scattering, Environ. Sci. Technol. 37 (2003) 5783–5791, https://doi.org/10.1021/es0300362.

[37] A. Cabrera Reina, L. Santos-Juanes, J.L. García Sánchez, J.L. Casas López, M. I. Maldonado Rubio, G. Li Puma, J.A. Sánchez Pérez, Modelling the photo-Fenton oxidation of the pharmaceutical paracetamol in water including the effect of photon absorption (VRPA), Appl. Catal. B: Environ. 166-167 (2015) 295–301, https://doi.org/10.1016/j.apcatb.2014.11.023.

[38] M.L. Satuf, R.J. Brandi, A.E. Cassano, O.M. Alfano, Experimental method to evaluate the optical properties of aqueous titanium dioxide suspensions, Ind. Eng. Chem. Res. 44 (2005) 6643–6649, https://doi.org/10.1021/ie050365y.

[39] J. Xi, H.S. Jung, Y. Xu, F. Xiao, J.W. Bae, S. Wang, Synthesis strategies, catalytic applications, and performance regulation of single-atom catalysts, Adv. Funct. Mater. 31 (2021) 2008318, https://doi.org/10.1002/adfm.202008318.

[40] Q. An, H. Zhang, N. Liu, S. Wu, S. Chen, Fe-doped g-C₃N₄ synthesized by supramolecular preorganization for enhanced photo-Fenton activity, Sep. Purif. Technol. 315 (2023) 123673, https://doi.org/10.1016/j.seppur.2023.123673.

[41] Z. Hu, X. Cai, Z. Wang, S. Li, Z. Wang, X. Xie, Construction of carbon-doped supramolecule-based g-C₃N₄/TiO₂ composites for removal of diclofenac and carbamazepine: a comparative study of operating parameters, mechanisms, degradation pathways, J. Hazard. Mater. 380 (2019) 120812, https://doi.org/10.1016/j.jhazmat.2019.120812.

[42] F. Xu, C. Lai, M. Zhang, D. Ma, L. Li, S. Liu, X. Zhou, H. Yan, N. Wang, M. Xu, L. Qin, H. Yi, Graphite carbon nitride coupled with high-dispersed iron (II) phthalocyanine for efficient oxytetracycline degradation under photo-Fenton process: performance and mechanism, Sep. Purif. Technol. 308 (2023) 122829, https://doi.org/10.1016/j.seppur.2022.122829.

[43] D.M. Zhao, C.-L. Dong, B. Wang, C. Chen, Y.-C. Huang, Z.D. Diao, S.Z. Li, L.J. Guo, S.H. Shen, Synergy of dopants and defects in graphitic carbon nitride with exceptionally modulated band structures for efficient photocatalytic oxygen evolution, Adv. Mater. 31 (2019) 1903545, https://doi.org/10.1002/adma.201903545.

[44] C. Han, L. Du, M. Konarova, D.-C. Qi, D.L. Phillips, J. Xu, Beyond hydrogen evolution: Solar-driven, water-donating transfer hydrogenation over platinum/carbon nitride, ACS Catal. 10 (2020) 9227–9235, https://doi.org/10.1021/acscatal.0c01932.

[45] W. Wang, X. Bai, Q. Ci, L. Du, X. Ren, D.L. Phillips, Near-field drives long-lived shallow trapping of polymeric C₃N₄ for efficient photocatalytic hydrogen evolution, Adv. Funct. Mater. 31 (2021) 2103978, https://doi.org/10.1002/adfm.202103978.

[46] G. Tamma, G. Valenti, Evaluating the oxidative stress in renal diseases: what is the role for S-glutathionylation? Antioxid. Redox Signal. 25 (2016) 147–164, https://doi.org/10.1089/ars.2016.6656.

[47] X.Y. Wang, J.Q. Meng, X.Y. Zhang, Y.Q. Liu, M. Ren, Y.X. Yang, Y.H. Guo, Controllable approach to carbon-deficient and oxygen-doped graphitic carbon nitride: robust photocatalyst against recalcitrant organic pollutants and the mechanism insight, Adv. Funct. Mater. 31 (2021) 2010763, https://doi.org/10.1002/adfm.202010763.

[48] Z. Sun, L. Zhu, Y. Liu, J. Wen, Degradation of 1,3,6,8-tetrabromocarbazole by sulfidated zero-valent iron activated peroxydisulfate: mechanistic insight and transformation pathways, Chem. Eng. J. 458 (2023) 141439, https://doi.org/10.1016/j.cej.2023.141439.

[49] Y. Chai, Y. Dai, X. Duan, Z. Sun, F. Hu, J. Qian, X. Peng, Elucidation of the mechanistic origin of spin-state-dependent P-doped Fe single-atom catalysts for the

oxidation of organic pollutants through peroxymonosulfate activation, Appl. Catal. B: Environ. 341 (2024) 123289, https://doi.org/10.1016/j.apcatb.2023.123289.

[50] X.-H. Yi, H. Ji, C.-C. Wang, Y. Li, Y.-H. Li, C. Zhao, A. Wang, H. Fu, P. Wang, X. Zhao, W. Liu, Photocatalysis-activated SR-AOP over PDINH/MIL-88A(Fe) composites for boosted chloroquine phosphate degradation: Performance,

mechanism, pathway and DFT calculations, Appl. Catal. B: Environ. 293 (2021) 120229, https://doi.org/10.1016/j.apcatb.2021.120229.

[51] Y. Chai, H. Dai, P. Zhan, Z. Liu, Z. Huang, C. Tan, F. Hu, X. Xu, X. Peng, Selective degradation of organic micropollutants by activation of peroxymonosulfate by Se@ NC: role of Se doping and nonradical pathway mechanism, J. Hazard. Mater. 452 (2023) 131202, https://doi.org/10.1016/j.jhazmat.2023.131202.